Research Paper

Thermal analysis of hybrid single-phase, two-phase and heat pump thermal control system (TCS) for future spacecraft

S.H. Lee [a], I. Mudawar [a,*], Mohammad M. Hasan [b]

[a] Boiling and Two-Phase Flow Laboratory (PU-BTPFL), School of Mechanical Engineering, Purdue University, 585 Purdue Mall, West Lafayette, IN 47907, USA
[b] NASA Glenn Research Center, 21000 Brookpark Road, Cleveland, OH 44135, USA

HIGHLIGHTS

- Hybrid Thermal Control System (H-TCS) is proposed for future spacecraft.
- Thermodynamic performance of H-TCS is examined for different space missions.
- Operational modes including single-phase, two-phase and heat pump are explored.
- R134a is deemed most appropriate working fluid.

ARTICLE INFO

ABSTRACT

An urgent need presently exists to develop a new class of versatile spacecraft capable of conducting different types of missions and enduring varying gravitational and temperature environments, including Lunar, Martian and Near Earth Object (NEOs). This study concerns the spacecraft's Thermal Control System (TCS), which tackles heat acquisition, especially from crew and avionics, heat transport, and ultimate heat rejection by radiation. The primary goal of the study is to explore the design and thermal performance of a Hybrid Thermal Control System (H-TCS) that would satisfy the diverse thermal requirements of the different space missions. The H-TCS must endure both 'cold' and 'hot' environments, reduce weight and size, and enhance thermodynamic performance. Four different operational modes are considered: single-phase, two-phase, basic heat pump and heat pump with liquid-side, suction-side heat exchanger. A thermodynamic trade study is conducted for six different working fluids to assess important performance parameters including mass flow rate of the working fluid, maximum pressure, radiator area, compressor/pump work, and coefficient of performance (COP). R134a is determined to be most suitable based on its ability to provide a balanced compromise between reducing flow rate and maintaining low system pressure, and a moderate coefficient of performance (COP); this fluid is also both nontoxic and nonflammable, and features zero ozone depletion potential (ODP) and low global warming potential (GWP). It is shown how specific mission stages dictate which mode of operation is most suitable, and this information is used to size the radiator for the H-TCS.

© 2016 Elsevier Ltd. All rights reserved.

1. Introduction

1.1. NASA's future space missions and associated boosters and space vehicles

Recently, budgetary constraints and policy changes have had a profound influence on future manned space missions, causing considerable uncertainty relative to which mission or missions would take precedence. For example, the NASA *Constellation Program* announced in 2005 included plans for a manned mission to the Moon by 2020 [1,2], asteroid in 2020 [3], and Mars by 2035 [4]. But in 2010, the U.S. cancelled the Constellation Program, abandoning plans for the Lunar mission and temporarily suspending plans for asteroid and Mars missions [5]. Nonetheless, the Constellation Program provided the most comprehensive plans for space exploration, and has already culminated in the development of rocket boosters and space vehicles that are expected to play crucial roles in future missions. These include two rocket boosters, Space Launch System (SLS) Crew and SLS Cargo, for launching crew and heavy hardware, respectively, into orbit [6,7]. The Constellation Program also included three space vehicles: (1) *Orion* Crew Exploration Vehicle (CEV) for deep space exploration, (2) *Altair* Lunar Surface Access Module (LSAM), for astronaut descent to, and ascend from the Moon, and (3) Earth Departure Stage (EDS), the main propulsion system for thrusting

Orion and Altair into Trans Lunar Trajectory from low Earth orbit [1].

1.2. Thermal control system (TCS) for future spacecraft

Faced with these mission uncertainties, there is now keen interest in developing a new class of versatile spacecraft, capable of conducting different types of missions and enduring varying gravitational and temperature environments, including Near Earth Objects (NEOs), Lunar surface, Martian surface, and deep space. This new paradigm is expected to impact virtually all systems comprising the spacecraft, including the Thermal Control System (TCS), which is responsible for maintaining acceptable temperature and humidity levels for both crew and avionics. The present study concerns the design of a TCS that is capable of tackling different missions and corresponding variations in the operating environment.

The TCS consists of components that tackle the spacecraft's *heat acquisition*, *transport*, and *rejection*. In a two-phase TCS, the heat is acquired via the TCS evaporator and rejected by radiation via the TCS condenser/radiator. The thermal load determines the amount of heat acquired by the evaporator, while the condenser temperature and effective heat sink temperature determine the heat flux at the condenser/radiator surface. The TCS tackles heat input from several sources, which include, in addition to crew metabolism and avionics, direct solar radiation and infrared radiation (IR) from, and fraction of solar radiation (albedo) reflected by, the Earth, Moon, Mars or asteroid. The heat load and effective heat sink temperature vary greatly, depending on mission destination and mission stages. For missions to Lunar and Martian surfaces, a variety of *active* TCS (*i.e.,* mechanically driven, as opposed to *passive* or surface tension driven heat pipe, capillary pumped loop, or loop heat pipe TCS) architectures have been proposed based on thermal load and requirements for different spacecraft, lander or habitat (*e.g.,* Lunar/Martian outpost lander and Lunar/Martian habitat) [4,8]. Because of increased heat load and closer temperature control requirements, future manned missions will require active TCS that is far more advanced than unmanned mission TCS.

Reducing weight and size of all components comprising the spacecraft, including the TCS, will be crucial to the success of any future manned space mission. An effective means to reducing the weight and size of an active TCS is to capitalize upon the latent heat of the working fluid, through evaporation and condensation, rather than on sensible heat alone. Trade studies by Ungar [9] and Ganapathi et al. [10] have shown that switching from single-phase to two-phase operation in high heat load missions can drastically reduce TCS weight and size.

1.3. Hybrid, reconfigurable thermal control system (TCS) for future spacecraft

The advantages of a two-phase pumped loop TCS are limited to 'cold' environments since the temperature of the working fluid must exceed the effective heat sink temperature to enable heat rejection from the condenser/radiator. For 'warm' environments, a vapor compression heat pump will be required to reject the heat. Ground experiments have demonstrated the effectiveness of vapor compression heat pumps in achieving high coefficient of performance (COP) and reducing mass flow rate of the working fluid for high thermal loads and warm environments [11–13].

To tackle the varying heat loads for different missions and both cold and warm environments, Singh and Hasan [14] proposed a 'hybrid', reconfigurable active TCS that uses a single working fluid. For cold environments, the TCS would operate as a mechanically pumped single-phase loop for low heat loads, or two-phase loop for high heat loads. For hot environments, the TCS would be reconfigured as a heat pump.

Aside from system concerns, several fundamental fluid physics considerations are expected to play a vital role in the development of a multi-mission or multi-environment hybrid TCS, especially in regard to flow passage diameter. Condensers and evaporators featuring small passage diameters produce higher flow velocities for given heat load and flow rate, yielding higher evaporation and condensation heat transfer coefficients [15] and greater insensitivity to varying gravitational field [16–18], let alone the reduction in system weight and size, provided these merits are realized without greatly increasing pressure drop. Furthermore, studies have shown that small diameter evaporators are compatible with standard heat pumps [19,20]. However, these advantages will be realized only if reliable predictive correlations and/or models are available for determination of evaporation and condensation pressure drops and heat transfer coefficients in reduced gravity.

1.4. Objectives of study

The primary objective of the present study is to explore the development of hybrid, reconfigurable TCS for a Multi-Purpose Crew Vehicle (MPCV) that can (1) be used in different mission types and mission stages, (2) endure both cold and hot environments, (3) resist sensitivity to varying gravitational field, (4) reduce weight and size, and (5) enhance both thermal and thermodynamic performances. A thermodynamic trade study will be conducted for different working fluids to assess important performance parameters, including mass flow rate of the working fluid, maximum pressure, condenser/radiator area, compressor/pump work, and COP. The hybrid TCS will capitalize upon the aforementioned benefits of small evaporator and condenser passage diameters. The study will also explore how the TCS must be reconfigured to tackle different missions and mission stages.

2. Mission description

2.1. Orion Multi-Purpose Crew Vehicle (MPCV)

Given the uncertainty concerning which space mission(s) would be undertaken in the foreseeable future, it is the primary goal of the present study to explore the design of a TCS that would satisfy thermal needs for trips to the Moon, Mars and NEO. The spacecraft for the missions described here are based on NASA's Constellation Program [1,3], with details of the Martian mission based on Design Reference Architecture 5.0 [4].

The system examined in this study is based on the Orion CEV. In its original form, this vehicle could be modified into different configurations in response to different mission needs: (i) CEV Block I for mission to the International Space Station (ISS) with a crew of six, crew rotation and maintenance supply, (ii) CEV Block II for lunar mission with a crew of four, and NEO mission with a crew of two to three, and (iii) CEV Block III for Martian mission with a crew of six [21,22]. The Orion CEV was renamed Orion MPCV after the cancellation of the Constellation Program and the mission to the ISS. The present study concerns TCS development for the Orion MPCV.

3. Hybrid TCS design

3.1. Thermal requirements and reconfigurable TCS

Future space missions will involve several complex stages and drastically different environments. The trips to the Moon, Mars or NEO will consist of various combinations of the mission stages outlined in Table 1. Shown in this table are the thermal loads and effective heat sink temperatures associated with the different mission stages, along with radiator surface emissivity, ε, and absorptivity, α, based on Altair [23]. The worst-case operating conditions for the

Table 1
Thermal loads and effective sink temperatures for different mission stages.

	Launch to LEO	TLC, TNEOC, TMC	LLO	LSO	NEO	MSO	LMO
Thermal load	1.2 kW	1 kW	5 kW	6.25 kW	TBD	6.25 kW	5 kW
Effective heat sink temperature	−93 to −66 °C (180 to 207K) (Altair) [23]	−198 °C (75K) (Altair) [23]	−213 to 17 °C (60 to 290K) (Altair) [23]	−56 to −34 °C (217 to 239K) (Altair) [23]	TBD	−123 to −23 °C (150 to 250K) (Orion) [14]	22 °C (295K) [24]
Radiator absorptivity	$\alpha = 0.1$ (Altair) [23]	$\alpha = 0.1$ (Altair) [23]	$\alpha = 0.1$ (Altair) [23]	$\alpha = 0.1$ (Altair) [23]			
Radiator emissivity	$\varepsilon = 0.85$ (Altair) [23]	$\varepsilon = 0.85$ (Altair) [23]	$\varepsilon = 0.85$ (Altair) [23]	$\varepsilon = 0.85$ (Altair) [23]			

Mission stage definition:
LEO: Low Earth Orbit; LLO: Low Lunar Orbit; TLC: Trans Lunar Coast; TNEOC: Trans Near Earth Objects Coast; TMC: Trans Mars Coast; LSO: Lunar Surface Operation; NEO: Near-Earth Object; MSO: Mars Surface Operation; LMO: Low Mars Orbit.

MPCV consist of a maximum thermal load of 6.25 kW, corresponding to Lunar Surface Operation (LSO), and maximum effective sink temperature of 295K for Low Mars Orbit (LMO). The maximum thermal load is comprised of two components: 5.5 kW from avionics and 0.75 kW from crew metabolism.

Because of its versatility in meeting the needs of most space missions, the MPCV is used in the present study as a reference system for evaluating the proposed single-loop Hybrid TCS (H-TCS). Once fully validated for the MPCV, the H-TCS concept could be expanded to higher thermal loads such as those encountered in Lunar and Martian habitats, with thermal loads of 50 and 25 kW, respectively [8].

The H-TCS loop configuration is shown in Fig. 1(a). This system is designed to accommodate three different operational modes: single-phase, two-phase and heat pump. The single-phase and two-phase modes are used in cold environments, while the heat pump is required for hot environments, where a compressor is needed to raise the fluid temperature above that of the heat sink.

3.2. Single-phase and two-phase modes

Figure 1(b) shows the H-TCS in the single-phase and two-phase modes. Heat is absorbed by cabin and avionics heat exchangers and rejected by the condenser/radiator. The cooling fluid is circulated by a gear pump, and an accumulator upstream of the cabin heat exchanger sets pressure for the entire loop. The loop mode is determined by fluid pressure in the cabin and avionics heat exchangers. In the single-phase mode, fluid pressure is higher than saturation pressure, and the temperature increases by up to 5 and 40 °C as the fluid exits the cabin and avionics heat exchangers, respectively [9]. In the two-phase mode, the working fluid maintains relatively constant saturation temperature and pressure as it absorbs the heat in both the cabin and avionics heat exchangers by changing phase. The condenser/radiator by-pass line is used to control the amount of heat rejected, which in turn maintains the temperature at the inlet to the cabin heat exchanger above 2 °C to protect the heat transport pipes and cabin heat exchanger from freezing and frost formation [10]. A liquid receiver tank stores liquid that is not in circulation and helps maintain constant pressure, and a venturi vacuum pump is used to remove any non-condensable gases from the fluid. The flow rate is measured by a turbine flow meter.

3.3. Heat pump mode

In the heat pump mode, Fig. 1(c), the same evaporators are used to extract the heat from the cabin and avionics. The mass flow rate of the working fluid is adjusted by a throttling valve in response to the temperature downstream of the avionics heat exchanger. To avoid the damaging influence of liquid droplets on compressor performance, the vapor is superheated by about 1 °C before entering the compressor. A small superheat also helps reduce the compressor's discharge temperature, and a 1 °C superheat has been

recommended for scroll type compressors [25]. The superheat is achieved either by adjusting the flow rate or utilizing a Liquid-Line Suction-Line Heat Exchanger (LLSL-HX). The LLSL-HX is a counter flow heat exchanger that transfers heat from hot liquid downstream of the condenser to cooler vapor downstream of the avionics heat exchanger, which helps enhance the cooling capacity of the evaporators. The vapor is supplied through a suction line accumulator before entering the compressor, which protects the compressor against liquid refrigerant flood-back. A scroll-type compressor is recommended because of its high tolerance to liquid droplets, with oil used for lubrication as well as for hermetic sealing to prevent refrigerant leakage [26]. Studies using the Ericsson cycle approximation for the heat pump cycle point to reduced compressor work when oil-flooding a scroll-type compressor, where the high heat capacity oil helps in absorbing heat from the refrigerant [27–29]. Oil flooding refers to using a large amount of oil, up to 55% of the oil-refrigerant mixture by mass for optimal COP; the oil is separated before the refrigerant enters the condenser [27]. For a conventional heat pump, optimal COP is achieved by injecting oil at 5% of the refrigerant flow rate [30]. The heat absorbed by the oil amounts to an inter-cooling effect, which helps reduce compressor work. The compressor increases the pressure and temperature of the vapor, and an oil separator downstream of the compressor removes the oil from the vapor. The hot vapor rejects heat to the ambient by the condensing radiator, and the vapor is converted to liquid downstream of the condenser. A liquid receiver tank is used as a pressure set point for the loop by providing sufficient storage volume to dampen pressure fluctuations. This pressure set point changes depending on the amount of refrigerant charged upstream of the throttling valve, and the liquid receiver tank minimizes variations in the mass flow by the cyclic operation of the compressor. Without the receiver tank, both the mass flow rate and pressure will vary significantly. A throttling valve is used to drop liquid pressure down to the pressure corresponding to the cabin heat exchanger's inlet; the liquid sometimes flashes into a two-phase mixture because of this pressure drop.

As discussed in the thermodynamic study below, each of the H-TCS modes (single-phase, two-phase and heat pump) will be optimal for one or more of the mission stages but not all stages. The thermodynamic trade study will explore optimal loop operation for different cooling loads and effective heat sink temperatures, and ascertain the need for H-TCS.

4. Requirements for different H-TCS modes

4.1. Working fluids

To determine the best working fluid for the different missions, six candidates, ammonia, R404a, R134a, R245fa, HFE7000 and R123 are investigated. These fluids have all been considered previously for spacecraft TCS and/or electronics thermal management, and their properties are summarized in Table 2.
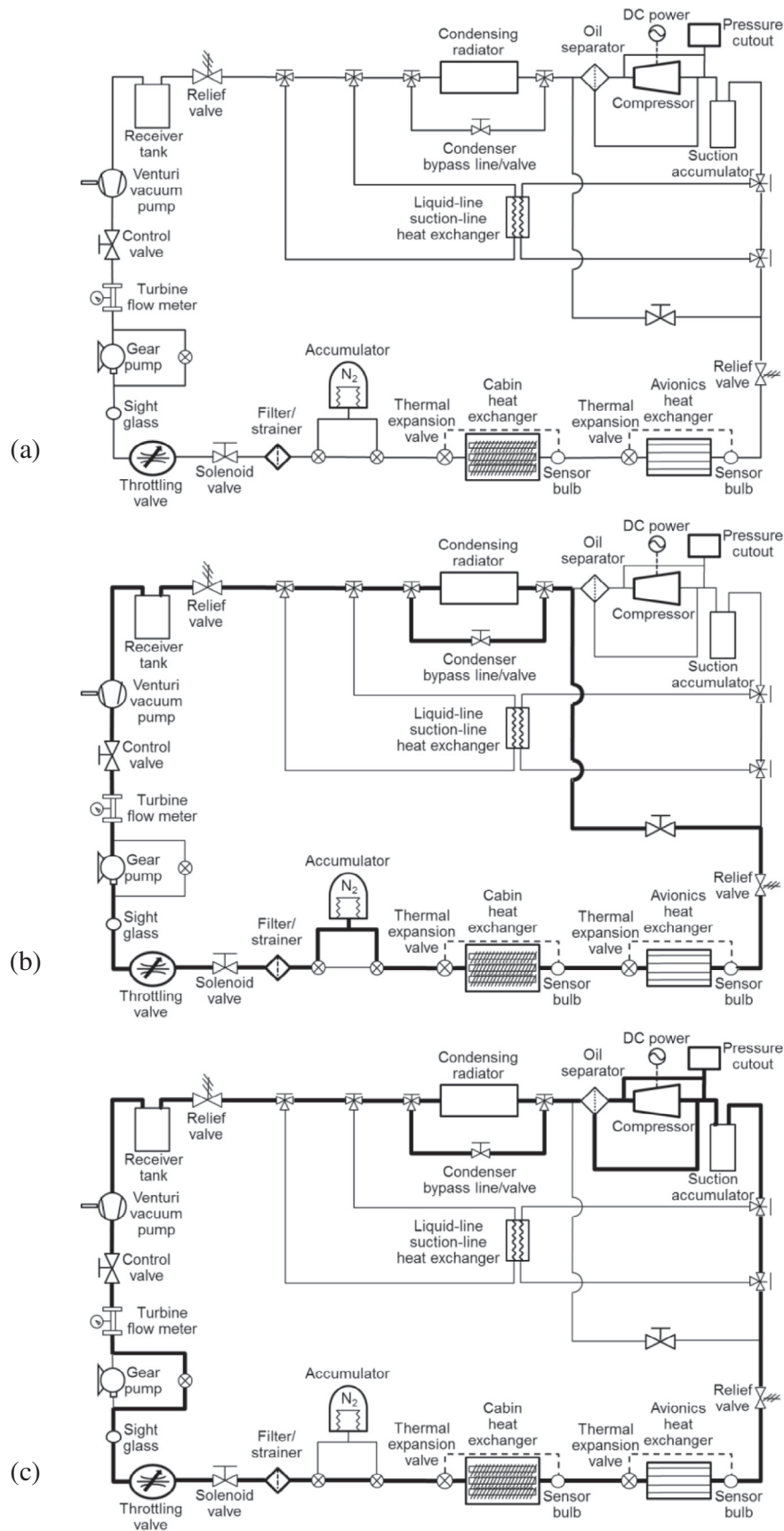
Fig. 1. (a) Layout of H-TCS. (b) Single-phase and two-phase loop configuration. (c) Heat pump configuration.

Table 2
Saturated thermophysical properties of candidate working fluids.

Reduced pressure P_r (P/P_{crit})	Sat. pressure P_{sat} (Pa)	Sat. temp. T_{sat} (°C)	Latent heat of vaporization h_{fg} (kJ/kg)	Liquid specific heat $c_{p,f}$ (kJ/kg.K)	Liquid density ρ_f (kg/m³)	Vapor density ρ_g (kg/m³)	Liquid viscosity μ_f (kg/m.s)	Liquid thermal conductivity k_f (W/m.K)	Liquid Prandtl number Pr_f	Surface tension σ (N/m)
Ammonia (P_{crit} = 11.33 MPa, T_{crit} = 132.25 °C (405.25K), ODP = 0, GWP = 0 (100 yr ITH))
8.94×10^{-3}	101.33×10^3	−33.33	1369.50	4.45	681.97	0.890	2.55×10^{-4}	6.66×10^{-1}	1.71	4.48×10^{-2}
1.0×10^{-2}	113.33×10^3	−31.07	1362.00	4.46	679.00	0.990	2.47×10^{-4}	6.58×10^{-1}	1.68	3.29×10^{-2}
5.0×10^{-2}	566.65×10^3	7.64	1234.00	4.66	628.10	4.52	1.57×10^{-4}	5.36×10^{-1}	1.36	2.37×10^{-2}
0.10	$1,133.30 \times 10^3$	29.01	1148.70	4.82	596.68	8.80	1.27×10^{-4}	4.74×10^{-1}	1.29	2.36×10^{-2}
0.30	$3,399.90 \times 10^3$	71.13	931.95	5.50	524.08	27.16	8.50×10^{-5}	3.60×10^{-1}	1.30	1.18×10^{-2}
0.50	$5,666.50 \times 10^3$	95.02	759.66	6.57	470.12	49.36	6.68×10^{-5}	2.98×10^{-1}	1.47	6.20×10^{-3}
0.70	$7,933.10 \times 10^3$	112.45	584.54	8.90	416.90	78.92	5.42×10^{-5}	2.52×10^{-1}	1.92	2.76×10^{-3}
0.90	$10,200.00 \times 10^3$	126.27	360.90	20.79	348.95	127.63	4.25×10^{-5}	2.17×10^{-1}	4.07	6.03×10^{-4}
R404a (P_{crit} = 3.73 Mpa, T_{crit} = 72.12 °C (345.12K), ODP = 0, GWP = 3922 (100 yr ITH))
1.0×10^{-2}	37.35×10^3	−65.42	211.60	1.18	1357.00	2.15	4.06×10^{-4}	9.84×10^{-2}	4.86	1.54×10^{-2}
2.7×10^{-2}	101.33×10^3	−46.22	200.94	1.25	1306.30	5.48	3.37×10^{-4}	9.20×10^{-2}	4.58	1.29×10^{-2}
5.0×10^{-2}	186.75×10^3	−32.88	191.40	1.27	1261.00	9.75	2.70×10^{-4}	8.73×10^{-2}	3.93	1.10×10^{-2}
0.10	373.48×10^3	−14.64	178.20	1.33	1203.30	19.05	2.17×10^{-4}	7.88×10^{-2}	3.67	9.30×10^{-3}
0.30	$1,120.40 \times 10^3$	20.77	145.40	1.51	1063.80	58.32	1.36×10^{-4}	6.52×10^{-2}	3.15	5.05×10^{-3}
0.50	$1,867.40 \times 10^3$	40.86	119.70	1.74	959.50	105.24	1.01×10^{-4}	5.77×10^{-2}	3.05	2.74×10^{-3}
0.70	$2,614.40 \times 10^3$	55.50	93.60	2.19	855.47	167.03	7.74×10^{-5}	5.22×10^{-2}	3.26	1.23×10^{-3}
0.90	$3,361.30 \times 10^3$	67.13	59.39	4.30	721.04	268.62	5.58×10^{-4}	4.95×10^{-2}	4.94	2.63×10^{-4}
R134a (P_{crit} = 4.06 MPa, T_{crit} = 101.06 °C (374.06K), ODP = 0, GWP = 1300 (100 yr ITH))
1.0×10^{-2}	40.59×10^3	−44.34	228.50	1.25	1430.00	2.23	4.99×10^{-4}	1.12×10^{-1}	5.58	1.83×10^{-2}
2.5×10^{-2}	101.32×10^3	−26.07	216.97	1.28	1376.70	5.26	3.79×10^{-4}	1.04×10^{-1}	4.67	1.54×10^{-2}
5.0×10^{-2}	202.95×10^3	−9.72	205.80	1.32	1327.00	10.15	3.02×10^{-4}	9.88×10^{-2}	4.02	1.30×10^{-2}
0.10	405.93×10^3	9.368	191.25	1.37	1263.10	19.81	2.37×10^{-4}	8.79×10^{-2}	3.69	1.02×10^{-2}
0.30	$1,217.80 \times 10^3$	46.89	155.44	1.54	1116.60	60.78	1.48×10^{-4}	7.18×10^{-2}	3.18	5.27×10^{-3}
0.50	$2,029.70 \times 10^3$	68.13	127.32	1.77	1007.50	109.61	1.10×10^{-4}	6.25×10^{-2}	3.11	2.81×10^{-3}
0.70	$2,841.50 \times 10^3$	83.60	98.76	2.23	899.31	173.71	8.37×10^{-5}	5.55×10^{-2}	3.36	1.27×10^{-3}
0.90	$3,653.40 \times 10^3$	95.85	61.79	4.37	758.70	278.57	6.04×10^{-5}	5.15×10^{-2}	5.13	2.76×10^{-4}
R245fa (P_{crit} = 3.65 MPa, T_{crit} = 154.01 °C (427.01K), ODP = 0, GWP = 950 (100 yr ITH))
1.0×10^{-2}	36.51×10^3	−7.82	208.68	1.26	1423.60	2.28	6.46×10^{-4}	9.83×10^{-2}	8.28	1.82×10^{-2}
2.8×10^{-2}	101.33×10^3	15.14	196.05	1.30	1364.90	5.96	4.63×10^{-4}	9.12×10^{-2}	6.61	1.53×10^{-2}
5.0×10^{-2}	182.55×10^3	30.75	186.88	1.33	1322.80	10.43	3.79×10^{-4}	8.63×10^{-2}	5.86	1.33×10^{-2}
0.10	365.10×10^3	51.94	173.33	1.39	1261.60	20.35	2.93×10^{-4}	7.95×10^{-2}	5.11	1.06×10^{-2}
0.30	$1,095.30 \times 10^3$	93.65	140.59	1.55	1119.10	62.18	1.78×10^{-4}	6.62×10^{-2}	4.17	5.51×10^{-3}
0.50	$1,825.50 \times 10^3$	117.30	115.22	1.74	1013.40	111.66	1.30×10^{-4}	5.92×10^{-2}	3.82	2.91×10^{-3}
0.70	$2,555.70 \times 10^3$	134.55	89.57	2.10	909.06	176.37	9.74×10^{-5}	5.48×10^{-2}	3.73	1.28×10^{-3}
0.90	$3,285.90 \times 10^3$	148.20	56.46	3.69	774.47	282.35	6.90×10^{-5}	5.33×10^{-2}	4.77	2.66×10^{-4}
HFE7000 (P_{crit} = 2.48 MPa, T_{crit} = 165.0 °C (438.0K), ODP = 0, GWP = 370 (100 yr ITH))
1.0×10^{-2}	24.78×10^3	5.0×10^{-1}	141.20	0.99	1481.00	2.22	6.66×10^{-4}	8.18×10^{-2}	9.7065	1.61×10^{-2}
4.1×10^{-2}	101.33×10^3	35.24	132.40	1.09	1385.00	8.34	4.24×10^{-4}	7.16×10^{-2}	7.3514	1.26×10^{-2}
5.0×10^{-2}	123.90×10^3	41.02	130.60	1.11	1368.00	10.09	3.94×10^{-4}	7.00×10^{-2}	7.0327	1.19×10^{-2}
0.10	247.79×10^3	62.87	123.20	1.18	1302.00	19.66	2.96×10^{-4}	6.40×10^{-2}	5.9643	9.77×10^{-3}
0.30	743.38×10^3	104.90	103.10	1.37	1153.00	60.01	1.64×10^{-4}	5.33×10^{-2}	4.3373	5.62×10^{-3}
0.50	$1,240.00 \times 10^3$	128.20	86.11	1.57	1048.00	107.60	1.10×10^{-4}	4.78×10^{-2}	3.5951	3.32×10^{-3}
0.70	$1,740.00 \times 10^3$	145.00	68.16	1.88	945.60	169.00	0.77×10^{-4}	4.42×10^{-2}	3.1538	1.69×10^{-3}
0.90	$2,230.00 \times 10^3$	158.40	44.29	2.92	813.00	267.70	0.50×10^{-4}	4.47×10^{-2}	3.3042	4.73×10^{-4}
R123 (P_{crit} = 3.66 MPa, T_{crit} = 183.68 °C (456.68K), ODP = 0.02, GWP = 120 (100 yr ITH))
1.0×10^{-2}	36.68×10^3	2.58	180.43	0.99	1519.80	2.50	5.47×10^{-4}	8.29×10^{-2}	6.55	1.79×10^{-2}
2.8×10^{-2}	101.32×10^3	27.82	170.19	1.02	1456.60	6.47	4.04×10^{-4}	7.56×10^{-2}	5.47	1.48×10^{-2}
5.0×10^{-2}	183.40×10^3	45.30	162.58	1.05	1410.60	11.33	3.32×10^{-4}	7.10×10^{-2}	4.90	1.28×10^{-2}
0.10	366.18×10^3	68.90	151.34	1.08	1344.40	21.99	2.59×10^{-4}	6.52×10^{-2}	4.28	1.02×10^{-2}
0.30	$1,098.50 \times 10^3$	115.68	123.64	1.19	1191.00	66.82	1.60×10^{-4}	5.48×10^{-2}	3.48	5.33×10^{-3}
0.50	$1,830.90 \times 10^3$	142.30	101.84	1.34	1077.10	119.63	1.21×10^{-4}	4.90×10^{-2}	3.29	2.89×10^{-3}
0.70	$2,563.30 \times 10^3$	161.73	79.51	1.63	963.68	188.22	9.44×10^{-5}	4.44×10^{-2}	3.46	1.32×10^{-3}
0.90	$3,295.60 \times 10^3$	177.13	50.22	2.99	815.42	299.78	7.06×10^{-5}	4.04×10^{-2}	5.23	2.96×10^{-4}

Thermophysical property sources:
• Ammonia, R404a, R134a, R245fa, R123: NIST REFPROP 8.0 [31].
• HFE7000: EES F-chart software [32].
ODP: Ozone Depletion Potential; GWP: Global Warming Potential; ITH: Integrated Time Horizon.

The candidate fluids are examined relative to four important performance parameters: required mass flow rate, maximum pressure, radiator area, and coefficient of performance (COP). For the heat pump configuration, the mass flow rate and COP influence power consumption, while maximum pressure dictates TCS weight via hardware mass and piping thickness. For the single-phase and two-phase modes, the mass flow rate influences pump work and TCS weight and size. Based on the thermal loads and effective sink temperatures provided in Table 1 for the different mission stages, the heat pump mode is evaluated only for Low Lunar Orbit (LLO) and Low Mars Orbit (LMO), whose highest sink temperatures exceed the lowest temperature of 2 °C at the inlet of the cabin heat exchanger. The single-phase or two-phase modes can be used in the LLO/LMO missions only when the sink temperature is lower than the heat acquisition temperature and the radiator area is large enough to reject the heat. The present thermodynamic study will examine all three H-TCS modes, single-phase, two-phase, and heat pump, subject to the operational parameters provided in Table 3.

4.2. Single-phase mode requirements

For the single-phase mode, Table 3 shows the minimum cabin heat exchanger's inlet temperature is set at $T_{cabinHX,in} = 2°C$ to prevent frost formation on the evaporator surfaces and control humidity level in the cabin [9]. The cabin reference temperature is set at $T_{cabin} = 10 °C$ and, to avoid any overheating of avionics, a maximum avionics heat exchanger outlet temperature at $T_{avionicsHX} = 40 °C$ [24]. With a pinch temperature difference between the cabin air temperature and cabin heat exchanger's fluid temperature of 5 °C, the maximum fluid temperature at the cabin heat exchanger's outlet is $T_{cabinHX,out} = 5°C$ to maintain adequate cabin heat exchanger heat transfer. As shown in Fig. 1(b), the cabin heat exchanger is situated upstream of the avionics heat exchanger, and the metabolic heat load is fixed at $Q_{cabinHX} = 0.75$ kW, while the avionics heat load, $Q_{avionicsHX}$, varies according to mission stage, from 0 to 5.5 kW. The temperature of the working fluid increases with increasing avionics heat load, and the mass flow rate $\dot{m}_{1\phi}$ for the single-phase mode is calculated from

$$\dot{m}_{1\phi} = Max\left\{\dot{m}_{cabinHX,1\phi}, \dot{m}_{avionicsHX,1\phi}\right\} \quad (1)$$

where

$$\dot{m}_{cabinHX,1\phi} = \frac{Q_{cabinHX}}{c_{p,f}(T_{cabinHX,out} - T_{cabinHX,in})} \quad (2a)$$

and

$$\dot{m}_{avionicsHX,1\phi} = \frac{Q_{avionicsHX}}{c_{p,f}(T_{avionicsHX,out} - T_{cavionicsHX,in})} \quad (2b)$$

Figure 2(a) shows the minimum mass flow rate for the different working fluids and different mission stages excepting Low Lunar Orbit (LLO) and Low Mars Orbit (LMO). Calculations reveal that the flow rate is determined by the cabin heat exchanger (i.e., Eq. (2a)) regardless of avionics heat load because of the small temperature rise allowed in the cabin heat exchanger. That is, the required mass flow rate of the cabin heat exchanger is always higher than that for the avionics heat exchanger. Because the flow rate is inversely proportional to specific heat, the flow rate is lowest for ammonia, followed by intermediate flow rates for R404a, R134a and R245fa, and highest flow rates for HFE7000 and R123.

To maintain liquid state in the entire single-phase loop, pressure must exceed saturation value corresponding to the highest temperature at the outlet of the avionics heat exchanger. Figure 2(b) shows the loop's lowest maximum pressure required for the different mission stages (excepting LLO and LMO) and different working fluids. At the highest avionics thermal load of 5.5 kW for Lunar Surface Operation (LSO) and Mars Surface Operation (MSO), R404a requires the highest pressure, 12.95 bar, corresponding to an

Table 3
Operational parameters for different H-TCS modes.

Mode	Cabin reference temp. set point T_{cabin}	Cabin heat exchanger minimum inlet temp. $T_{cabinHX,in}$	Cabin heat exchanger maximum outlet temp. $T_{cabinHX,out}$	Avionics heat exchanger maximum outlet temp. $T_{avionics,out}$	Evaporator temp. rise ΔT_{evap}	Compressor inlet superheat ΔT_{super}	Pinch temp. difference ΔT_{pinch}	Compressor efficiency η_{comp}	LLSL-H/X regeneration effectiveness ε_{reg}	Radiator absorptivity α	Radiator emissivity ε
Single-phase	10 °C (283K)	2 °C (275K)	5 °C (278K)	40 °C (313K)	3–38 °C (3–38K)	N/A	5 °C (5K)	NA	NA	0.1	0.85
Two-phase	10 °C (283K)	2 °C (275K)	5 °C (278K)	5 °C (278K)	0–3 °C (0–3K)	N/A	5 °C (5K)	NA	NA	0.1	0.85
Heat pump	10 °C (283K)	2–5 °C (275–278K)	5 °C (275–278K)	6 °C (279K)	1–4 °C (1–4K)	1 °C (1K)	5 °C (5K)	85%	0.9	0.1	0.85

Two-Phase mode maximum avionics heat exchanger temperature: $T_{avionicsHX,out} = T_{evap,sat}$.
Heat Pump mode maximum avionics heat exchanger temperature: $T_{avionicHX,out} = T_{evap,sat} + T_{super}$.
Evaporator temperature rise: $\Delta T_{evap} = T_{avionicsHX,out} - T_{cabinHX,in}$ for single-phase mode.
Cabin heat exchanger pinch temperature difference: $\Delta T_{pinch} = T_{cabin} - T_{cabinHX,out}$.
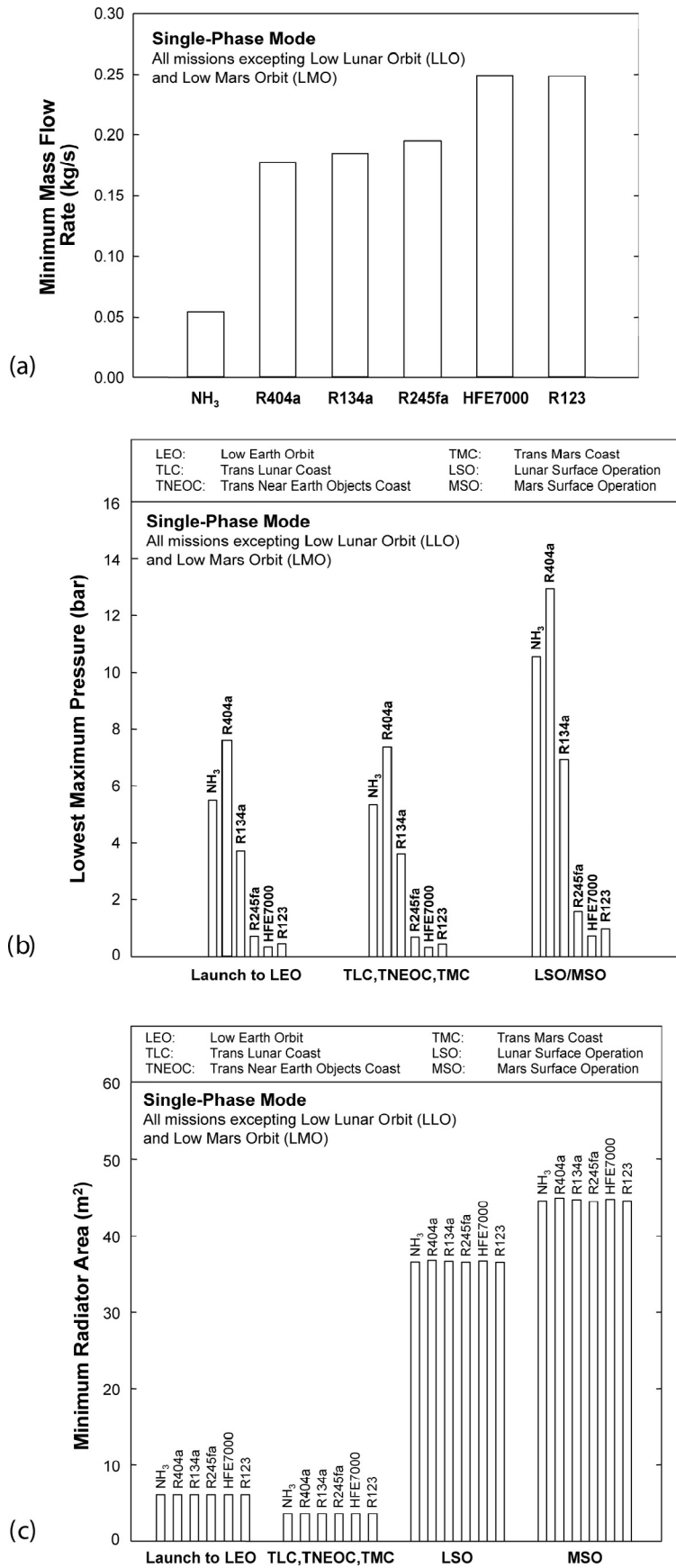
Fig. 2. Requirements for single-phase mode: (a) minimum flow rate, (b) lowest maximum pressure, and (c) minimum radiator area.

avionics heat exchanger outlet temperature of 26.07 °C. Notice that the maximum allowable avionics temperature of 40 °C is never reached for any of the conditions examined. A key drawback to high pressure is increased wall thickness of TCS tubing, which, as suggested by Ungar [9], drastically increases the weight of a single-phase TCS utilizing long tubing.

The required radiator area is calculated by the Stefan–Boltzmann law with the gray surface assumption ($\alpha = \varepsilon$),

$$A_{radiator} = \frac{Q_{cabinHX} + Q_{avionicsHX}}{\varepsilon\sigma\left(T_{radiator,s}^4 - T_{sink}^4\right)} = \frac{\dot{m}_{1\varphi}c_{p,f}\left(T_{avionicsHX,out} - T_{cabinHX,in}\right)}{\varepsilon\sigma\left(T_{radiator,s}^4 - T_{sink}^4\right)} \quad (3)$$

where $\sigma = 5.67 \times 10^{-8}$ W/m^2.K^4. The radiator surface temperature in Eq. (3) is approximated as

$$T_{radiator,s} = \frac{T_{cabinHX,in} + T_{avionicsHX,out}}{2} \quad (4)$$

Figure 2(c) shows the minimum radiator area required for all missions excepting LLO and LMO. Notice that the area is about same for the different working fluids because the avionics heat exchanger outlet temperatures corresponding to the highest area value for $Q_{avionicsHX}$ are quite close, 6.79 °C (R404a) to 9.76 °C (R134a) for Launch to LEO, 5.99 °C (R404a) to 8.97 °C (R134a) for TLC/TNEOC/TMC, and 26.07 °C (R404a) to 29.20 °C (R134a) for LSO/MSO. Therefore, radiator area is not an important factor in selecting working fluid for the single-phase mode.

4.3. Two-phase mode requirements

For the two-phase mode, the cabin temperature is set at 10 °C, and the fluid is assumed to enter the cabin heat exchanger as single-phase liquid at 2 °C. Using a cabin pinch temperature of 5 °C, the highest cabin heat exchanger outlet temperature is 5 °C. Like the single-phase mode, the cabin heat exchanger heat load is fixed at $Q_{cabinHX} = 0.75$ kW, while the avionics heat load, $Q_{avionicsHX}$, is allowed to vary according to mission stage, from 0 to 5.5 kW. Calculations reveal that the working fluid changes phase within the cabin heat exchanger for all mission stages.

The minimum mass flow rate is based on the assumption that the fluid exits the avionics heat exchanger in saturated vapor state, hence the total cooling capacity is set equal to the enthalpy difference between saturated two-phase flow ($x_e = 1$) at the outlet of the avionics heat exchanger and single-phase liquid at 2 °C at the inlet to the cabin heat exchanger.

$$\dot{m}_{2\phi} = \frac{Q_{cabinHX} + Q_{avionicsHX}}{c_{p,f}\left(T_{avionicsHX,out} - T_{cabinHX,in}\right) + h_{fg}} \quad (5)$$

The mass flow rate is evaluated for different saturation temperatures ranging from 2 to 5 °C in the cabin heat exchanger. Because of the higher enthalpy of saturated vapor at 5 °C compared to 2 °C, the minimum mass flow rate corresponds to saturation temperature of 5 °C. This also implies that the fluid maintains two-phase flow within the avionics heat exchanger at a constant temperature of 5 °C. The mass flow rate is calculated according to Eq. (5) with $T_{cabinHX,in} = 2$ °C, $T_{avionicsHX,out} = 5$ °C, and $Q_{avionicsHX} = 5.5$ kW. Figure 3(a) shows the minimum mass flow rate required for the two-phase mode. For all missions shown, the flow rate is smallest for ammonia and highest for HFE7000. Notably, because the two-phase mode relies on sensible and latent heat rather than on sensible heat alone, the required mass flow rates for the two-phase mode are considerably smaller than those shown in Fig. 2(a) for the single-phase mode. The two-phase mode reduces the flow rate to a mere 18.0% of the single-phase value for LSO/LMO, 3.6% for LEO, and 3.2% for TLC.

Figure 3(b) shows the loop's lowest maximum pressure required for the two-phase mode, which is set equal to the saturation temperature corresponding to a maximum avionics heat exchanger outlet temperature of 5 °C. Here, R404a requires the highest pressure, followed by ammonia, while HFE7000 requires the lowest pressure. Comparing these results to those in Fig. 2(b) shows maximum pressure for the two-phase mode is smaller than for the single-phase mode.

The minimum radiator area required for the two-phase mode must account for both sensible and latent heat. The condensing radiator area is the sum of two portions, two-phase and single-phase. In the upstream two-phase portion, the fluid rejects all its latent heat at $T_{sat} = T_{avionicsHX,out} = 5$ °C, and the radiator surface temperature is approximated at $T_{avionicsHX,out}$. For the downstream single-phase portion, the fluid temperature drops from $T_{avionicsHX,out} = 5$ °C to $T_{cabinHX,in} = 2$ °C, and the radiator surface temperature $T_{radiator,s}$ is approximated according to Eq. (4). Therefore, the total radiator area is given by

$$A_{radiator} = \dot{m}_{2\varphi}\left\{\frac{h_{fg}}{\varepsilon\sigma\left(T_{avionicsHX,out}^4 - T_{sink}^4\right)} + \frac{c_{p,f}\left(T_{avionicsHX,out} - T_{cabinHX,in}\right)}{\varepsilon\sigma\left(T_{radiator,s}^4 - T_{sink}^4\right)}\right\}$$
$$(6)$$

Because this area is based on total heat input and identical cabin heat exchanger inlet and avionics heat exchanger outlet temperatures, the required area for a given mission stage is almost fluid independent as reflected in Fig. 3(c). Comparing results from Fig. 3(c) to those in Fig. 2(c) shows that, because of lower radiator surface temperatures, the two-phase mode requires larger radiator area compared to the single-phase mode.

4.4. Heat pump mode requirements

The heat pump mode is considered for only two situations: (1) where the sink temperature is higher than the lowest temperature of 2 °C at the inlet of the cabin heat exchanger, and (2) for missions with heat sink temperatures below 2 °C where heat rejection with the single-phase and two-phase modes is not possible because of insufficient radiator area.

For LEO, TLC/TNEOC/TMC, LSO and MSO missions, where the heat sink temperature is lower than the fluid temperature in the cabin and avionics heat exchangers, the mass flow rates required for the heat pump mode are equal to those for the two-phase mode if the superheating effect is neglected. Here, the fluid enters the cabin heat exchanger as subcooled liquid at 2 °C with a saturation temperature of 5 °C.

The high heat sink temperatures for LLO and LMO will necessitate heat pump mode use, and the fluid flow rate must be determined separately for these two missions. For both LLO and LMO, the working fluid enters the cabin heat exchanger as a two-phase mixture. As indicated in Table 1, the heat load is same for LLO and LMO, but the condenser's outlet temperature will be different because of different heat sink temperatures. Considering a pinch temperature difference of 5 °C at the condenser outlet to maintain adequate condenser heat transfer performance, the condenser's outlet temperature will be 22 °C for LLO and 27 °C for LMO.

Figure 4(a) shows the minimum mass flow rate for the different working fluids in the heat pump mode for LLO and LMO, where cooling capacity is determined by enthalpy difference between the condenser's outlet and avionics heat exchanger exit. Hot liquid exiting the condenser is converted into a lower temperature two-phase mixture at the same enthalpy as a result of pressure drop across the throttling valve. Because of lower condenser outlet temperature for LLO, the enthalpy at the inlet to the cabin heat exchanger is lower and the evaporator enthalpy rise is higher for LLO
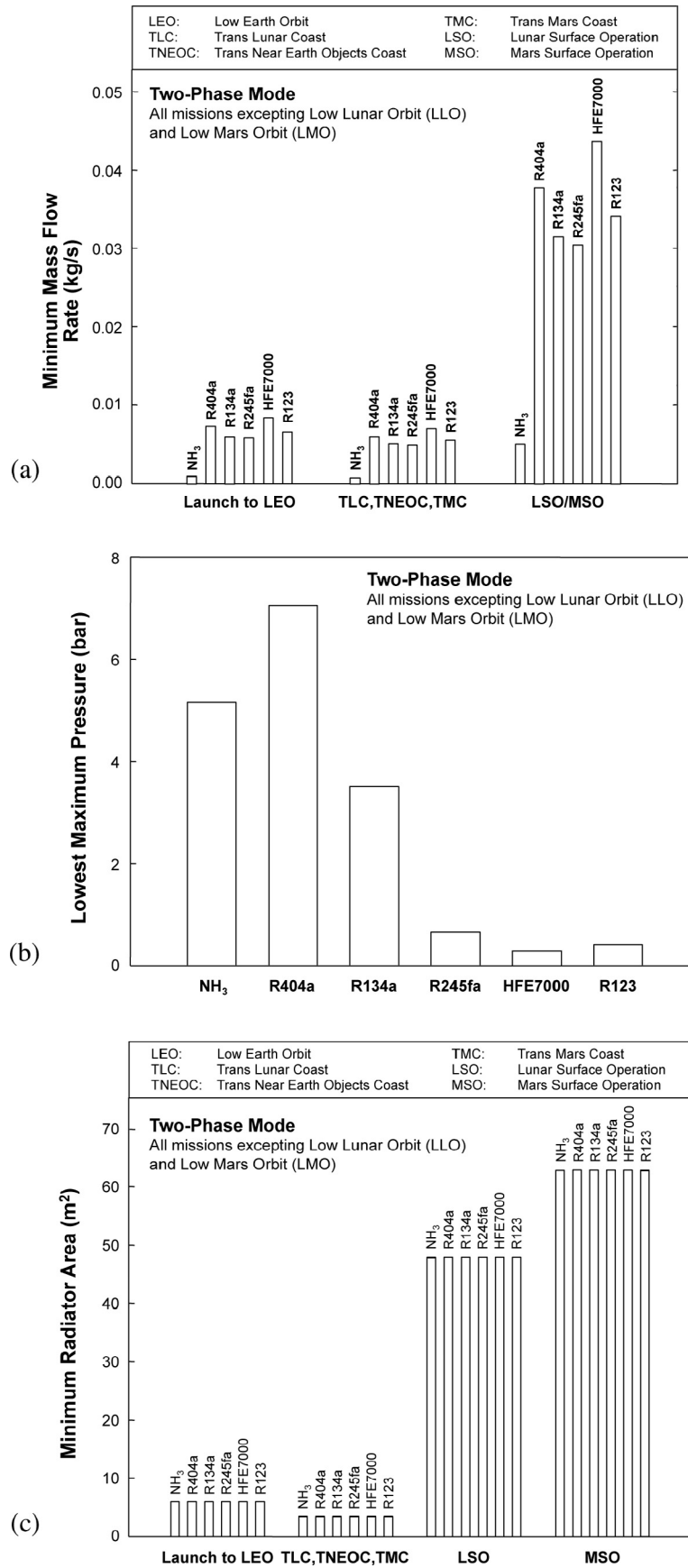
Fig. 3. Requirements for two-phase mode: (a) minimum flow rate, (b) lowest maximum pressure, and (c) minimum radiator area.
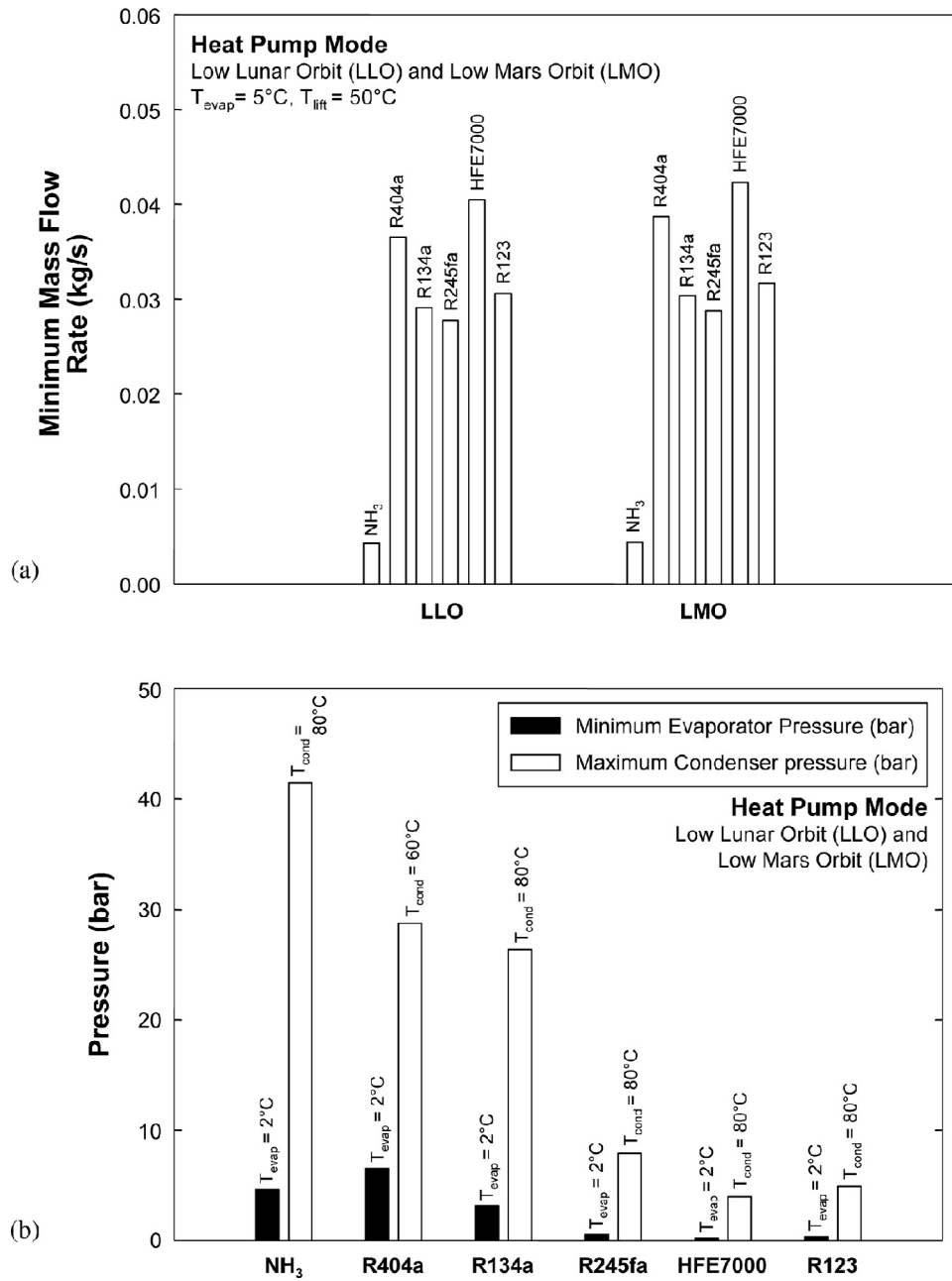
Fig. 4. Requirements for heat pump mode: (a) minimum flow rate, and (b) maximum and minimum pressures.

compared to LMO. This implies that, despite equal thermal loads, the mass flow rate for LLO is lower than for LMO as shown in Fig. 4(a). Having the highest latent heat, ammonia requires the lowest flow rate, followed by R245fa and R134a.

Figure 4(b) shows the maximum condenser pressure and minimum evaporator pressure for the heat pump corresponding to LLO and LMO. The maximum condenser pressure corresponds to the condenser's saturation temperature, which is the sum of evaporation temperature and temperature lift across the compressor, and the minimum evaporator pressure as the saturation pressure corresponding to the minimum evaporator temperature of 2 °C. Excepting R404a, a condenser saturation temperature of 80 °C is used to preclude exceeding the critical temperature for R134a. Because of its relatively low critical temperature of 72.07 °C, the maximum pressure for R404a is based on a maximum condenser temperature of 60 °C rather than 80 °C. Figure 4(b) shows that, despite the

advantage of lowest flow rate, ammonia will require higher pressure than all the other fluids.

The radiator area for the heat pump is comprised of three portions: superheated vapor, two-phase mixture, and single-phase liquid.

$$A_{radiator,s} = A_{vapor} + A_{sat} + A_{liquid} \tag{7}$$

$$\text{where} \quad A_{vapor} = \frac{\dot{m}_{hp}c_{p,f}\left(T_{cond,in} - T_{cond,sat}\right)}{\varepsilon\sigma\left\{\left(\frac{T_{cond,in} + T_{cond,sat}}{2}\right)^4 - T_{sink}^4\right\}} \tag{8a}$$

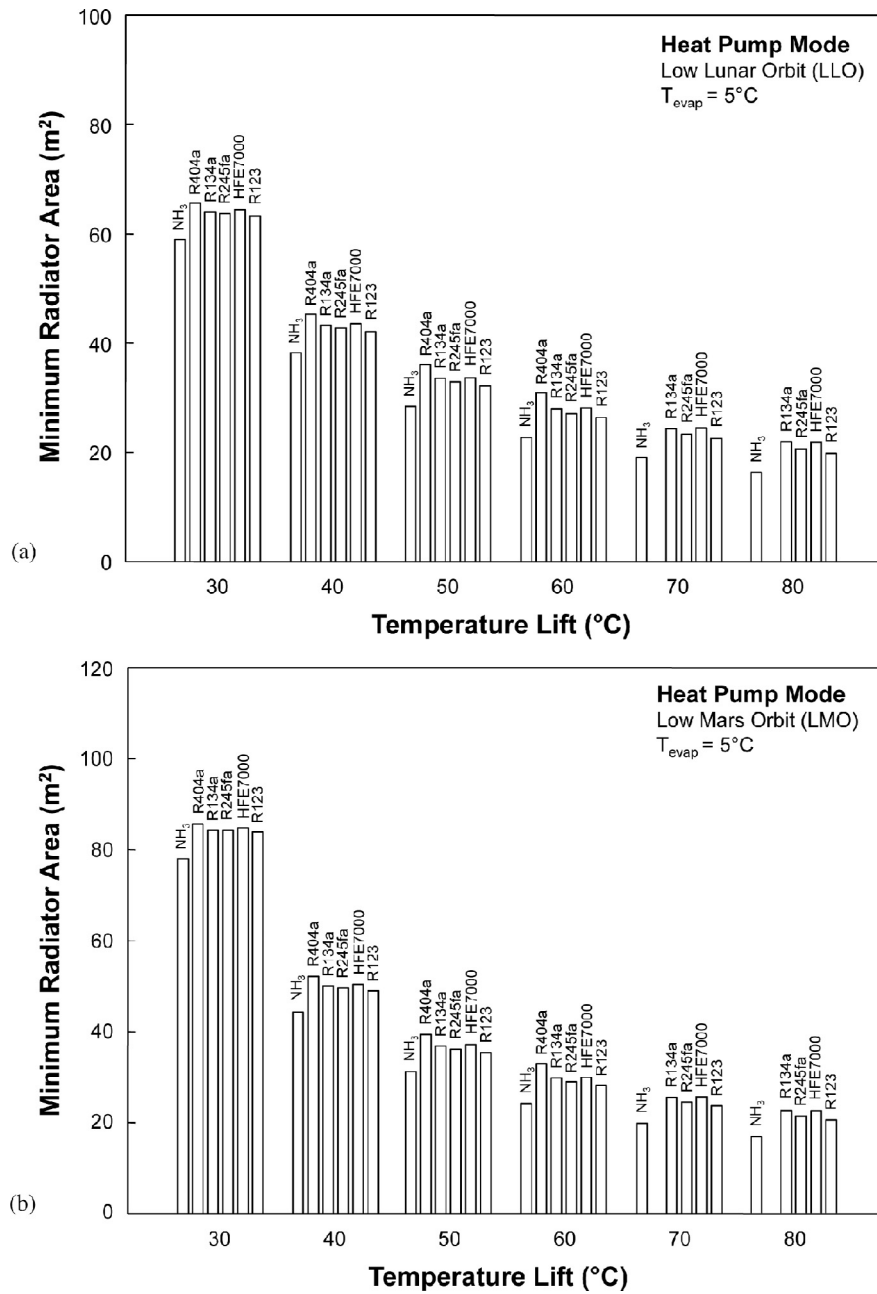$$A_{sat} = \frac{\dot{m}_{hp}h_{fg}}{\varepsilon\sigma\left\{T_{cond,sat}^4 - T_{sink}^4\right\}} \tag{8b}$$

Fig. 5. Minimum radiator area for heat pump mode for: (a) Low Lunar Orbit (LLO) and (b) Low Mars Orbit (LMO).

$$A_{liquid} = \frac{\dot{m}_{hp}c_{p,f}\left(T_{cond,sat} - T_{cond,out}\right)}{\varepsilon\sigma\left\{\left(\frac{T_{cond,sat} + T_{cond,out}}{2}\right)^4 - T_{sink}^4\right\}} \qquad (8c)$$

and $\quad T_{cond,sat} = T_{evap} + T_{lift}$ \hfill (9)

Figure 5(a) and (b) shows radiator area predictions for the different fluids and lift temperatures of 30 to 80 °C for LLO and LMO, respectively. Because of the relatively low critical temperature of 72.07 °C for R404a, no area results are provided for this fluid for the two highest lift temperatures. Overall, Figs. 5(a) and 5(b) shows that ammonia requires the smallest radiator area, but area differences among the different fluids are not significant. Despite requiring the smallest area, ammonia requires very high condenser pressure as shown in Fig. 4(b).

Coefficient of performance (COP) calculations are performed for the heat pump mode based on several assumptions. COP and compressor work are defined, respectively, as

$$COP = \frac{Q_{cabinHX} + Q_{avionicsHX}}{W_{comp}} \qquad (10)$$

and $\quad W_{comp} = \int_{P_{avionicsHX,out}}^{P_{cond,in}} VdP = \dot{m}_{hp}\left(h_{cond,in} - h_{avionicsHX,out}\right)$ \hfill (11)

The present study ignores compressor efficiency differences for different fluids by assuming an identical isentropic efficiency value of $\eta_{comp} = 85\%$ [24]. It is assumed that the fluid is superheated 1 °C at the avionics heat exchanger outlet to make certain that it enters
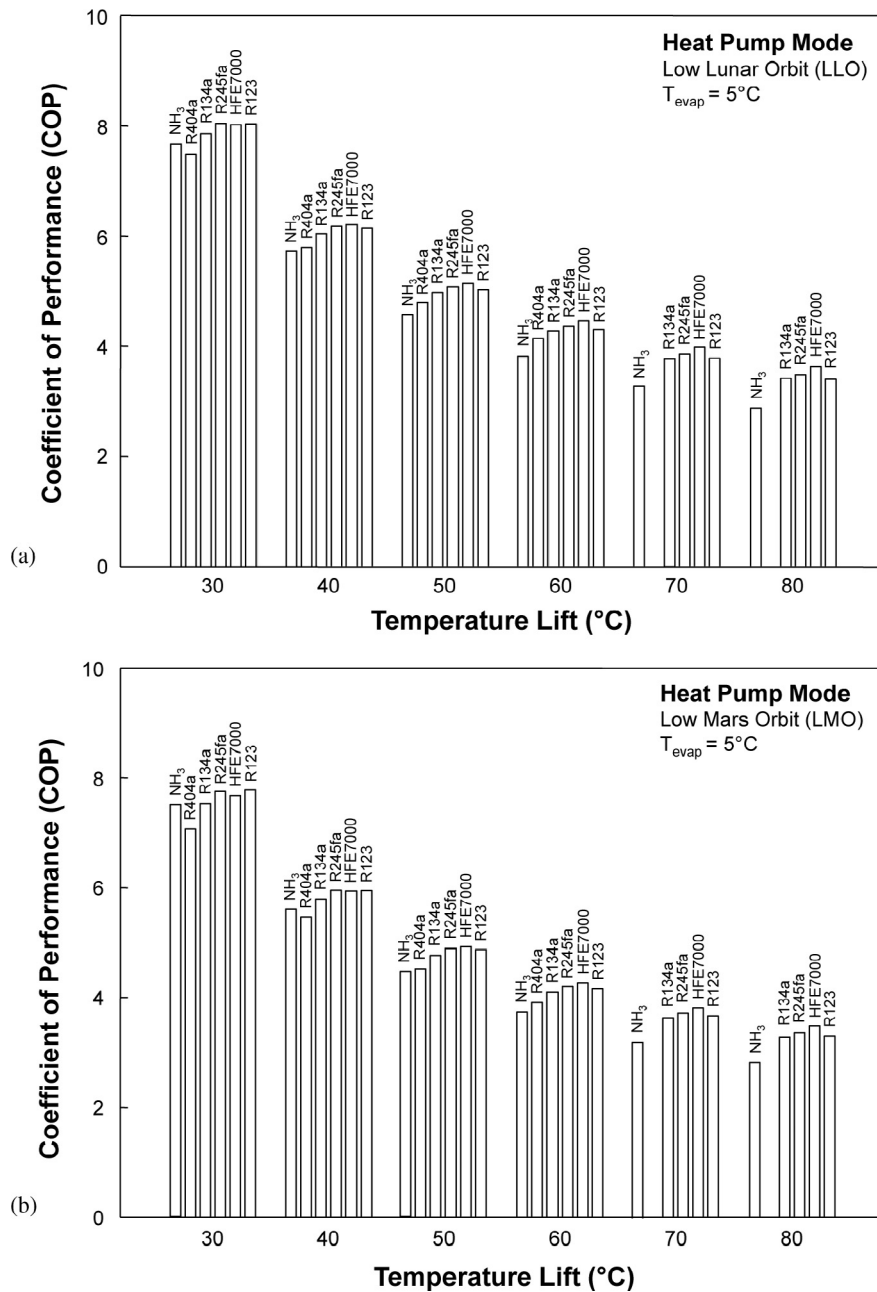
Fig. 6. Coefficient of performance (COP) for heat pump mode for: (a) Low Lunar Orbit (LLO) and (b) Low Mars Orbit (LMO).

the compressor as superheated vapor. Calculations are performed for a temperature lift from the avionics heat exchanger outlet ranging from 30 to 80 °C. Despite requiring the lowest flow rate, ammonia requires the highest compressor work in temperature lifts higher than 40 °C and 50 °C for LLO and LMO, respectively, because of high saturation pressure in the condenser. Figure 6(a) and (b) shows COP results for LLO and LMO missions, respectively. Notice the superior performance for LLO brought about by the lower cabin heat exchanger's inlet enthalpy. For both LLO and LMO, COP decreases with increasing temperature lift because of the higher enthalpy increase and compressor work. Overall, COP differences for the different mission stages and different fluids at a fixed temperature lift are relatively small.

4.5. Pressure drop and volumetric capacity concerns

Pressure drop is another important practical concern in any two-phase system, including heat pump. As liquid is converted to vapor in the evaporator, it causes acceleration of the fluid because of the drastic reduction in the fluid density. Pressure drop is comprised of three components: friction, acceleration, and gravity. The accelerational pressure drop greatly increases in magnitude compared to friction and gravity for small diameter tubing, which is desired in TCS, especially for high heat flux avionics [33,34]. Using the Homogeneous Equilibrium Model (HEM) [33,34], the accelerational pressure drop is obtained by integrating
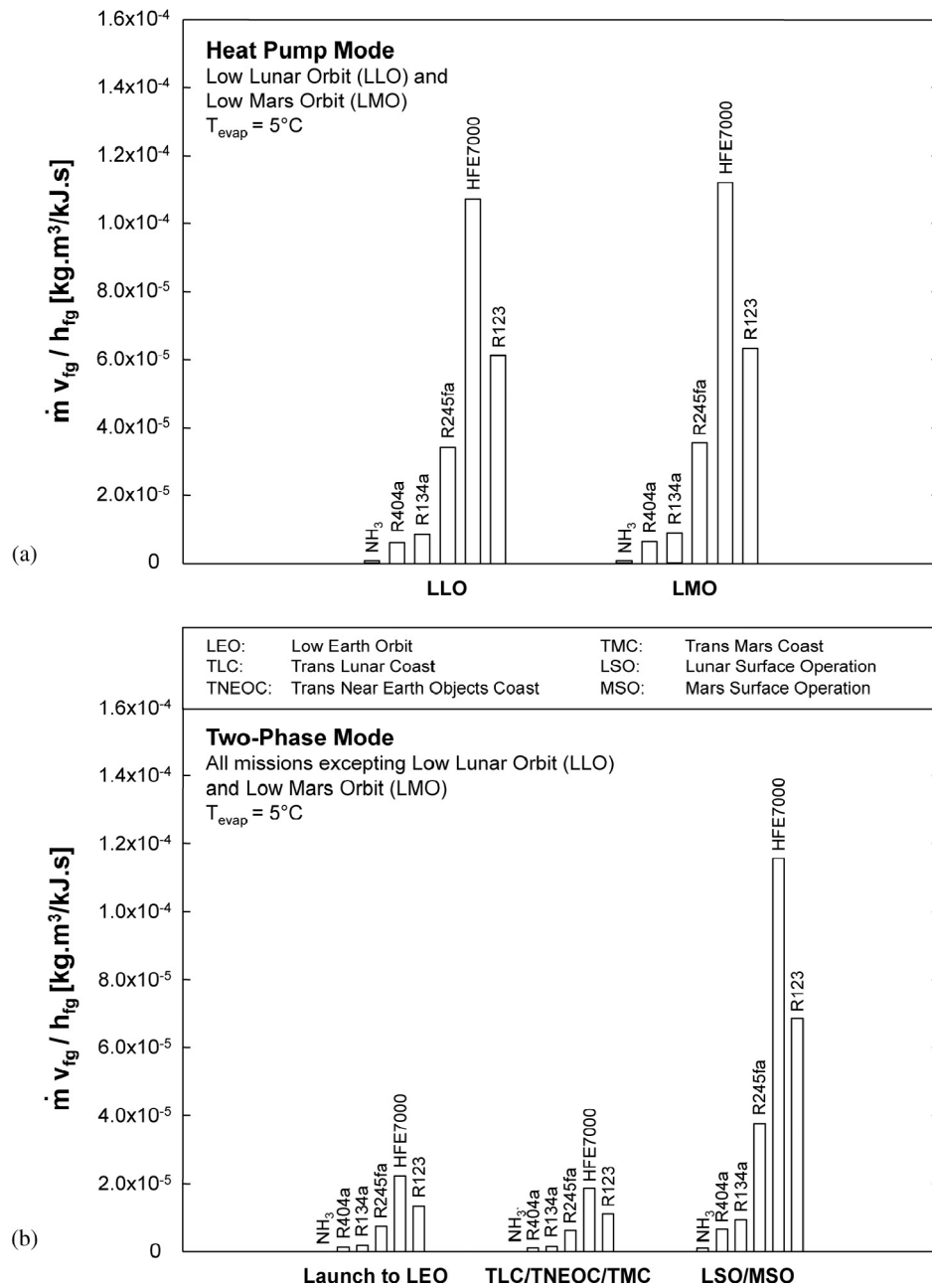
Fig. 7. Accelerational pressure drop parameter for different missions and fluids for (a) heat pump mode and (b) two-phase mode.

$$-\left(\frac{dP}{dz}\right)_A = \left[\frac{\dot{m}}{\left(\frac{\pi D^2}{4}\right)}\right]^2 v_{fg}\frac{dx_e}{dz} \qquad (12)$$

over the length of the evaporator tubing, where

$$\frac{dx_e}{dz} = \frac{q'}{\dot{m}h_{fg}} \qquad (13)$$

and q' is the heat transfer rate per tube length. Combining Eqs. (12) and (13) yields

$$-\left(\frac{dP}{dz}\right)_A = \frac{1}{\left[\left(\frac{\pi D^2}{4}\right)\right]^2}\left(\frac{\dot{m}v_{fg}}{h_{fg}}\right)q' \qquad (14)$$

For a given q', tube length, and tube diameter, the acclerational pressure drop is proportional to the parameter $\dot{m}v_{fg}/h_{fg}$. Figure 7(a) shows, for the heat pump mode and both LLO and LMO, the magnitude of this parameter at an evaporator saturation temperature of 5 °C. The accelerational pressure drop parameter is highest for HFE7000 because of its relatively high specific volume difference, $v_{fg} = 0.3714$ m^3/kg, and low latent heat of vaporization, $h_{fg} = 140.7$ kJ/kg, at 5 °C. On the other hand, ammonia has the lowest accelerational pressure drop parameter value because of its high latent heat,

Table 4

Mass flow rate and accelerational pressure drop parameter values for two-phase and heat pump modes corresponding to different mission stages and different fluids.

Operation mode	Parameter	NH$_3$	R404a	R134a	R245fa	HFE7000	R123
Two-phase mode and heat pump mode (T_{evap} = 5 °C)	v_{fg} (m^3/kg)	2.41×10^{-1}	2.71×10^{-2}	5.76×10^{-2}	2.49×10^{-1}	3.71×10^{-1}	3.61×10^{-1}
	h_{fg} (kJ/kg)	1244.0	161.0	194.8	201.7	140.2	179.9
Two-phase mode (T_{evap} = 5 °C)	Mass flow rate (kg/s) (Launch to LEO)	9.54×10^{-4}	7.26×10^{-3}	6.03×10^{-3}	5.84×10^{-3}	8.38×10^{-3}	6.56×10^{-3}
	Mass flow rate (kg/s) (TLC/TNEOC/TMC)	7.95×10^{-4}	6.05×10^{-3}	5.03×10^{-3}	4.87×10^{-3}	6.98×10^{-3}	5.47×10^{-3}
	Mass flow rate (kg/s) (LSO/MSO)	4.97×10^{-3}	3.78×10^{-2}	3.14×10^{-2}	3.04×10^{-2}	4.36×10^{-2}	3.42×10^{-2}
	Pressure drop parameter (kg.m^3/s.kJ) (Launch to LEO)	1.84×10^{-7}	1.22×10^{-6}	1.78×10^{-6}	7.21×10^{-6}	2.22×10^{-5}	1.32×10^{-5}
	Pressure drop parameter (kg.m^3/s.kJ) (TLC/TNEOC/TMC)	1.54×10^{-7}	1.02×10^{-6}	1.49×10^{-6}	6.01×10^{-6}	1.85×10^{-5}	1.10×10^{-5}
	Pressure drop parameter (kg.m^3/s.kJ) (LSO/MSO)	9.61×10^{-7}	6.38×10^{-6}	9.30×10^{-6}	3.76×10^{-5}	1.16×10^{-4}	6.85×10^{-5}
Heat pump mode (T_{evap} = 5 °C, T_{lift} = 50 °C)	Mass flow rate (kg/s) (LLO)	4.29×10^{-3}	3.66×10^{-2}	2.91×10^{-2}	2.77×10^{-2}	4.05×10^{-2}	3.06×10^{-2}
	Mass flow rate (kg/s) (LMO)	4.38×10^{-3}	3.88×10^{-2}	3.04×10^{-2}	2.88×10^{-2}	4.23×10^{-2}	3.16×10^{-2}
	Pressure drop parameter (kg.m^3/s.kJ) (LLO)	8.30×10^{-7}	6.17×10^{-6}	8.61×10^{-6}	3.43×10^{-5}	1.07×10^{-4}	6.14×10^{-5}
	Pressure drop parameter (kg.m^3/s.kJ) (LMO)	8.47×10^{-7}	6.53×10^{-6}	8.98×10^{-6}	3.56×10^{-5}	1.12×10^{-4}	6.34×10^{-5}

h_{fg} = 1244 kJ/kg, and low mass flow rate, 4.29×10^{-3} kg/s for LLO and 4.38×10^{-3} kg/s for LMO.

Figure 7(b) shows values of the acceleration pressure drop parameter for the two-phase loop and different mission stages. Here, the value of this parameter increases with increases in mission heat load and mass flow rate. Detailed values of the accelerational pressure drop parameter for both the two-phase and heat pump modes, different fluids and different mission stages are provided in Table 4.

Figure 7(a) and (b) suggests the pressure drop parameter is crucial for determining optimum working fluid for different TCS heat loads. This is especially the case for H-TCS that would be used later for a large system such as the lunar habitat, with a heat load of 50 kW [8]. Table 4 shows that, for all missions, the value of the pressure drop parameter is about twelve times smaller for R134a than for HFE7000 in all mission stages, which is the result of the high specific volume of HFE7000 brought about by its low reduced pressure.

However, HFE7000 is considered a viable fluid candidate because it requires low pressures as shown in Figs. 2(b) and 3(b), which is beneficial to reducing TCS mass. This fact is illustrated by comparing, for the heat pump mode and LLO, P-v diagrams for R134a and HFE7000, as shown in Figure 8(a) and (b), respectively. Notice that saturated vapor specific volume is highest at the compressor inlet, point 4. One measure of system volume is *volumetric capacity*, which is defined as evaporator heat load per unit volume of fluid being circulated.

$$q_v = \frac{Q_{cabinHX} + Q_{avionicsHX}}{V_4} = \frac{\dot{m}_{hp}(h_{avionicsHX,out} - h_{cabinHX,in})}{\dot{m}v_4} = \frac{h_4 - h_1}{v_4} \quad (15)$$

Volumetric capacity is an important factor in compressor selection and sizing. It is therefore examined here for the heat pump mode for LLO and LMO, as shown in Fig. 9(a). HFE7000 is shown requiring low volumetric capacity because of its high specific volume, but it also requires the highest volumetric flow rate at the compressor inlet as shown in Fig. 9(b), and therefore the largest compressor volume. This should also impact accumulator volume for the single-phase and two-phase modes.

4.6. Optimum working fluid

Comparing the requirements for the different fluids points to several important trends. Figures 2(a), 3(a) and 4(a) show that ammonia requires the smallest flow rates; however, Figs. 2(b), 3(b) and 4(b) also show this fluid requires very high condenser pressure. The trends for HFE7000 and R123 are opposite to those for ammonia, requiring the highest flow rates but low condenser pressures. R404a requires very high pressures without the benefit of reduced flow rate, while R134a and R245fa provide a compromise between reducing flow rate and maintaining low condenser pressure. As indicated earlier, radiator area is fairly similar for different fluids, Fig. 5(a) and (b), therefore this parameter is not important to fluid selection. Figure 6(a) and (b) shows COP values for the different fluids are also close. Figure 7(a) and (b) shows HFE7000 may pose adverse accelerational pressure drop effects, let alone high volume requirements, Figure 9(a) and (b).

But another important concern in selecting working fluid is safety. As indicated in Table 5, ammonia is the only fluid with flammability concerns, and ammonia, R245fa and R123 exhibit some toxicity. Three fluids exhibit no toxicity and no flammability, R404a, R134a, and HFE7000.

Another important concern is environmental impact. The 1987 Montreal Protocol resulted in gradual phaseout of ozone-depleting refrigerants, starting with chlorofluorocarbons (CFCs) (*e.g.,* R11, R12, R113, R114 and R115), which consist of chlorine, fluorine and carbon atoms, and afterwards with hydrochlorofluorocarbons (HCFCs) (*e.g,* R22, R123, R124 and R142b), which consist of hydrogen, chlorine, fluorine and carbon atoms [35]. Overall, HCFCs have far smaller, albeit finite, Ozone Depletion Potential (ODP) compared to CFCs. The gradual phaseout of refrigerants prompted many industries to seek replacements for specific coolants. For example, R11 was replaced by R123, but reduced ODP of the latter came at the expense of a 5% reduction in coefficient of performance (COP) [36]. A third family of refrigerants, hydrofluorocarbons (HFCs), which consist of hydrogen, fluorine and carbon atoms, are presently favored for their zero ODP as well as low Global Warming Potential (GWP) [37]. Collectively nicknamed "super greenhouse gases," HFCs include four of the six fluids considered in the present study, R404a, R134a, R245fa, and HFE7000, which were developed as replacements to specific CFCs and HCFCs.

As discussed above, R134a and R245fa provide a compromise between reducing flow rate and maintaining low condenser pressure; they also provide moderate COP values. This explains why previous TCS studies have employed both R134a [12,14,38] and R245fa [23]. However, because of toxicity concerns with R245fa, the present study will focus on R134a, whose chemical name and chemical formula are 1,1,1,2-Tetrafluoroethane and CH_2FCF_3, respectively. Low toxicity and good thermal attributes also explain why R134a is widely used in domestic refrigeration and automobile air-conditioning.
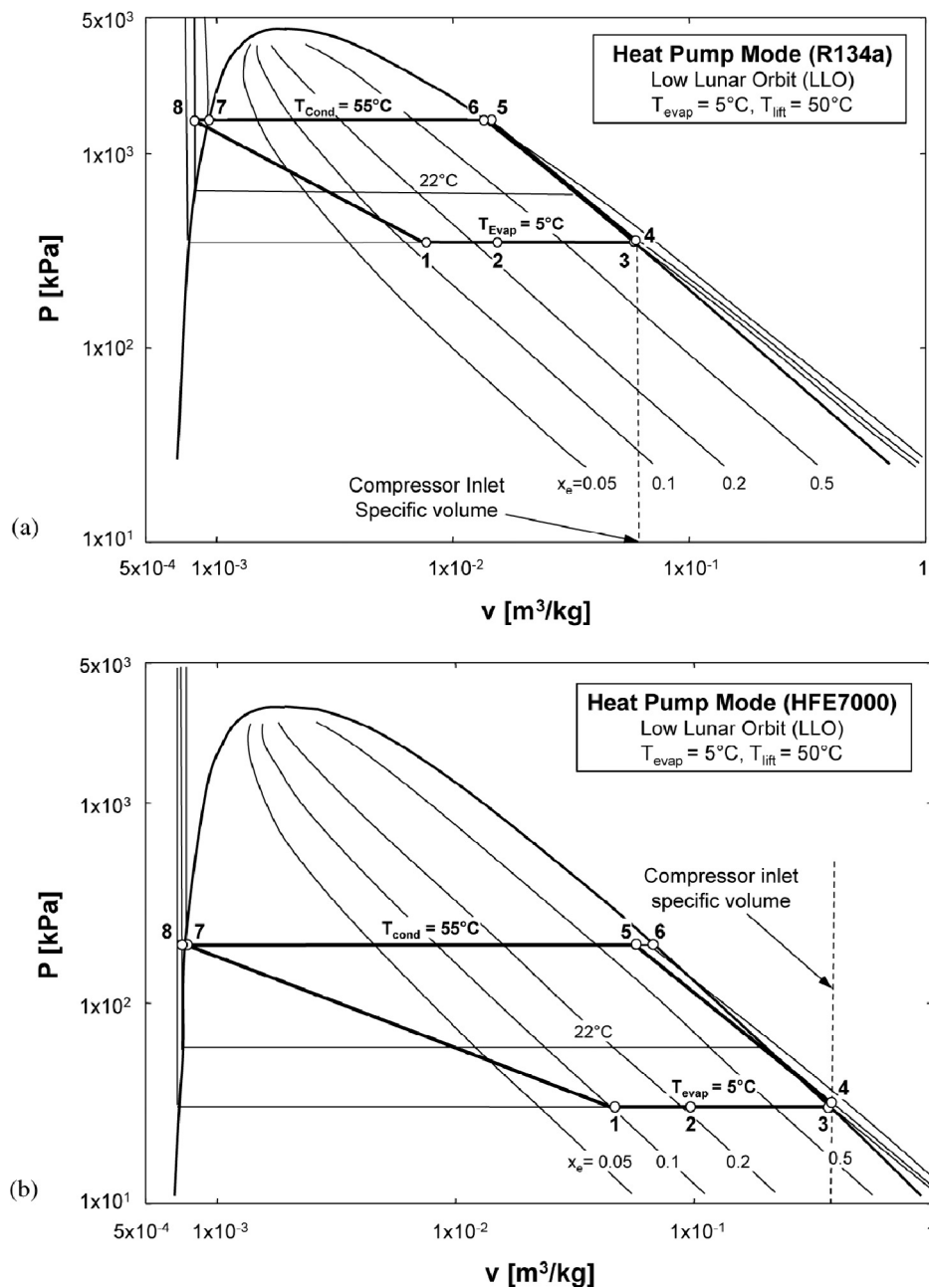
Fig. 8. *P-v* diagram for heat pump mode for LLO using (a) R134a and (b) HFE7000.

5. Thermodynamic analysis for H-TCS using R134a

5.1. Thermodynamic analysis for single-phase mode using R134a

All prior spacecraft have employed single-phase liquid TCSs, which feature loop simplicity and reliability, as well as adequate insensitivity to varying gravitational field. However, the single-phase mode suffers two critical disadvantages when managing high heat loads, high mass flow rate and high pressure. A high heat load causes appreciable temperature rise along the avionics heat exchanger. And the outlet temperature of the avionics heat exchanger determines saturation pressure, which sets pressure requirements for the entire loop since pressure in the single-phase mode must be maintained above saturation. Figure 10 shows the avionics heat exchanger outlet temperature and corresponding saturation pressure for the different mission stages (excepting LLO and LMO)

using R134a. As indicated earlier, the spacecraft TCS is commonly designed to prevent the avionics heat exchanger outlet temperature from exceeding 40 °C, and Fig. 10 shows this goal is met even at the maximum heat load associated with LSO and MSO, yet pressure is quite elevated.

5.2. Thermodynamic analysis for two-phase mode using R134a

In the two-phase mode, the working fluid enters the cabin heat exchanger 2 °C subcooled and is converted to a two-phase mixture as it absorbs heat from the cabin and avionics. The two-phase heat acquisition occurs at a saturation temperature ranging from 2 to 5 °C, and the fluid exits the avionics heat exchanger as saturated vapor ($x_e = 1$). Fluid circulation is achieved with a gear pump located downstream from the condenser as shown in Fig. 1(b), and pressure is pre-set by an accumulator and regulated by a control valve.
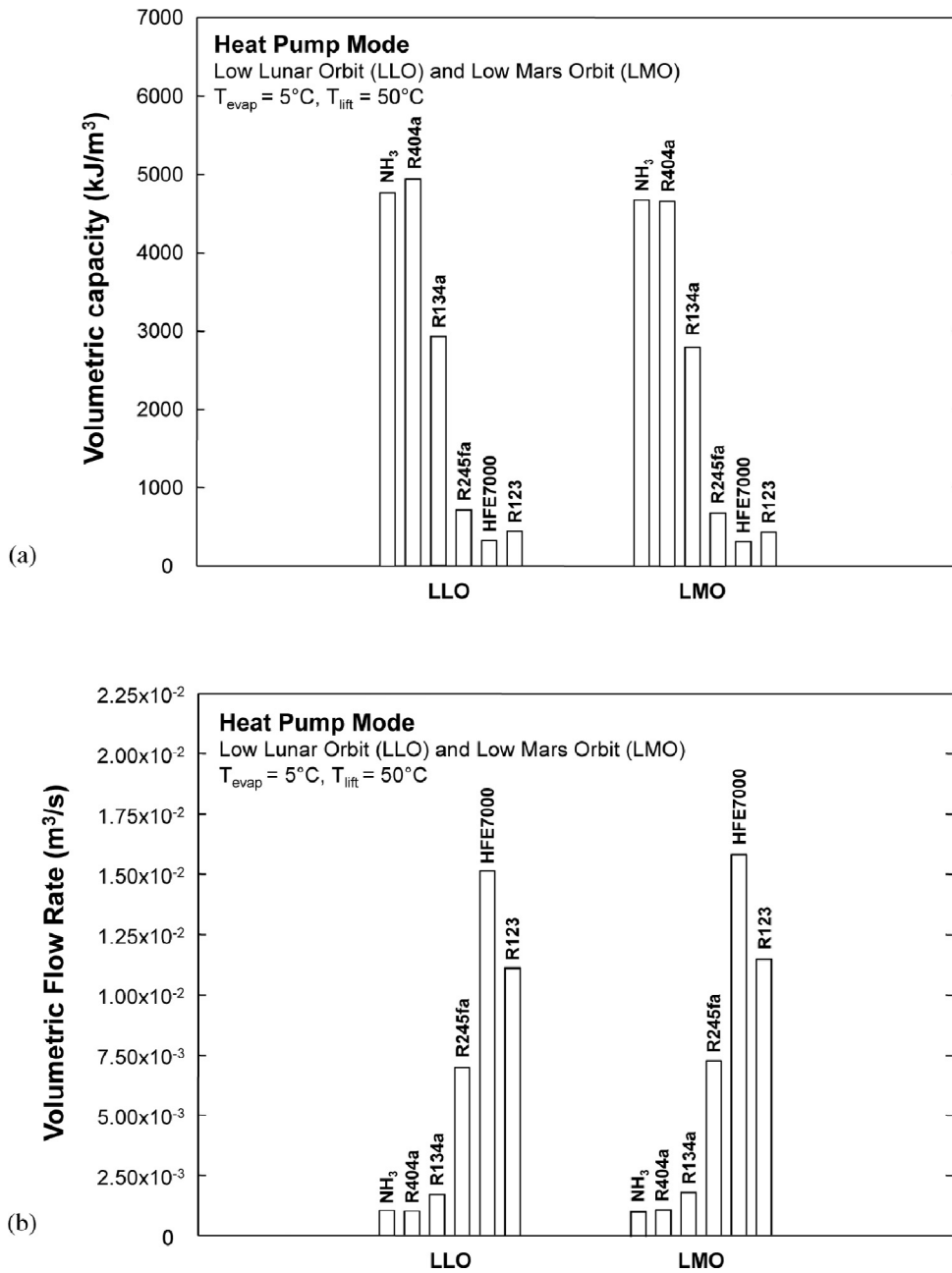
Fig. 9. (a) Volumetric capacity and (b) volumetric flow rate for heat pump mode and LLO and LMO mission stages for different working fluids.

Figure 11(a) shows the required flow rate for R134a versus evaporation temperature in the range of 2 to 5 °C for Launch to LEO and TLC/TNEOC/TMC; Fig. 11(b) shows a similar plot for LSO/MSO. The flow rate decreases monotonically with increasing saturation temperature, from 6.09×10^{-3} to 6.04×10^{-3} kg/s for Launch to LEO, 5.07×10^{-3} to 5.03×10^{-3} kg/s for TLC/TNEOC/TMC, and 3.17×10^{-2} to 3.14×10^{-2} for LSO/MSO; the latter requires the highest flow rates to tackle the highest heat load of 6.25 kW.

Figure 11(c) shows a *P-h* diagram for R134a for LSO/MSO. The indicated horizontal span is a measure of the evaporator's cooling capacity. Notice how increasing the evaporator's saturation temperature from 2 to 5 °C increases enthalpy change by $\Delta h = 1.694$ kJ/kg and therefore decreases the required flow rate for the same inlet temperature of 2 °C and same heat load. The ratio of cabin to total heat load of 0.75 to 6.25 kW sets the location of the cabin heat exchanger's outlet in Fig. 11(c).

Table 5
Safety ratings of candidate working fluids.

	Rating
Ammonia	B2
R404a	A1
R134a	A1
R245fa	B1
HFE7000	A1
R123	B1

Toxicity Rating:
Class A: no evidence of toxicity below 400 ppm.
Class B: evidence of toxicity below 400 ppm.
Flammability Rating:
Class 1: no flame propagation in open air.
Class 2: may propagate flame under certain conditions in open air.
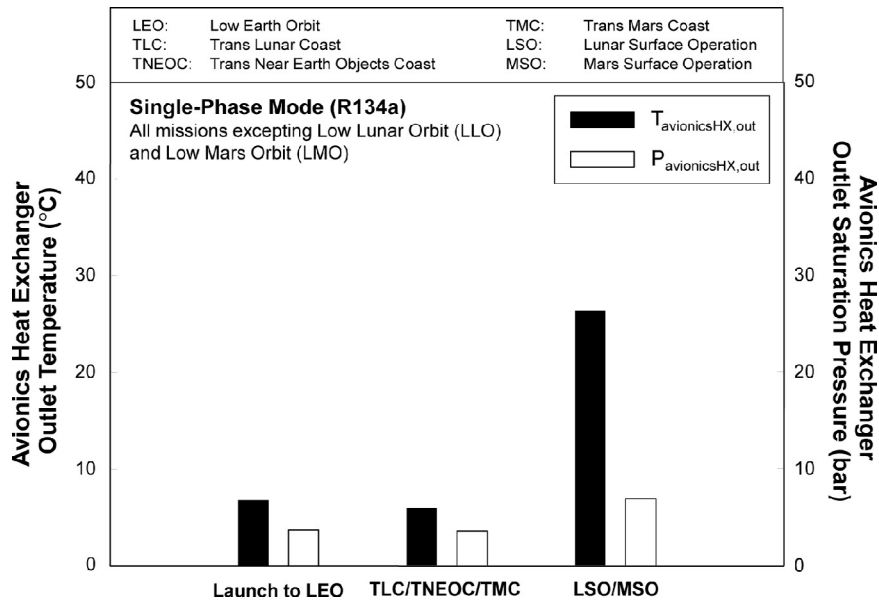Class 3: highly flammable.

Fig. 10. Avionics heat exchanger outlet temperature and corresponding saturation pressure for single-phase mode using R134a.
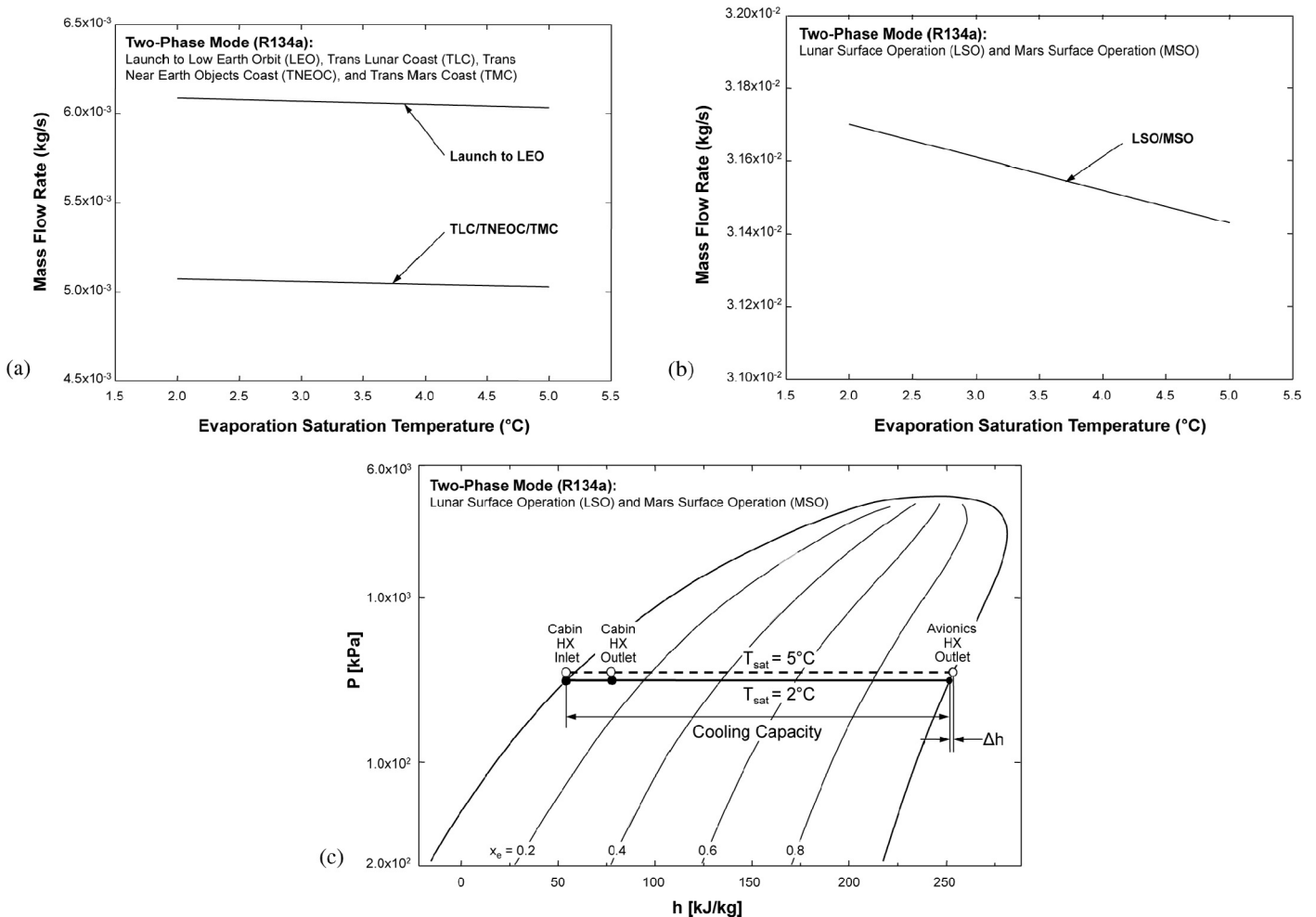

Fig. 11. Variation of required flow rate with evaporation saturation temperature for two-phase mode using R134a for (a) Launch to LEO and TLC/TNEOC/TMC, and (b) LSO/MSO. (c) P-h diagram for two-phase mode using R134a for LSO/MSO.
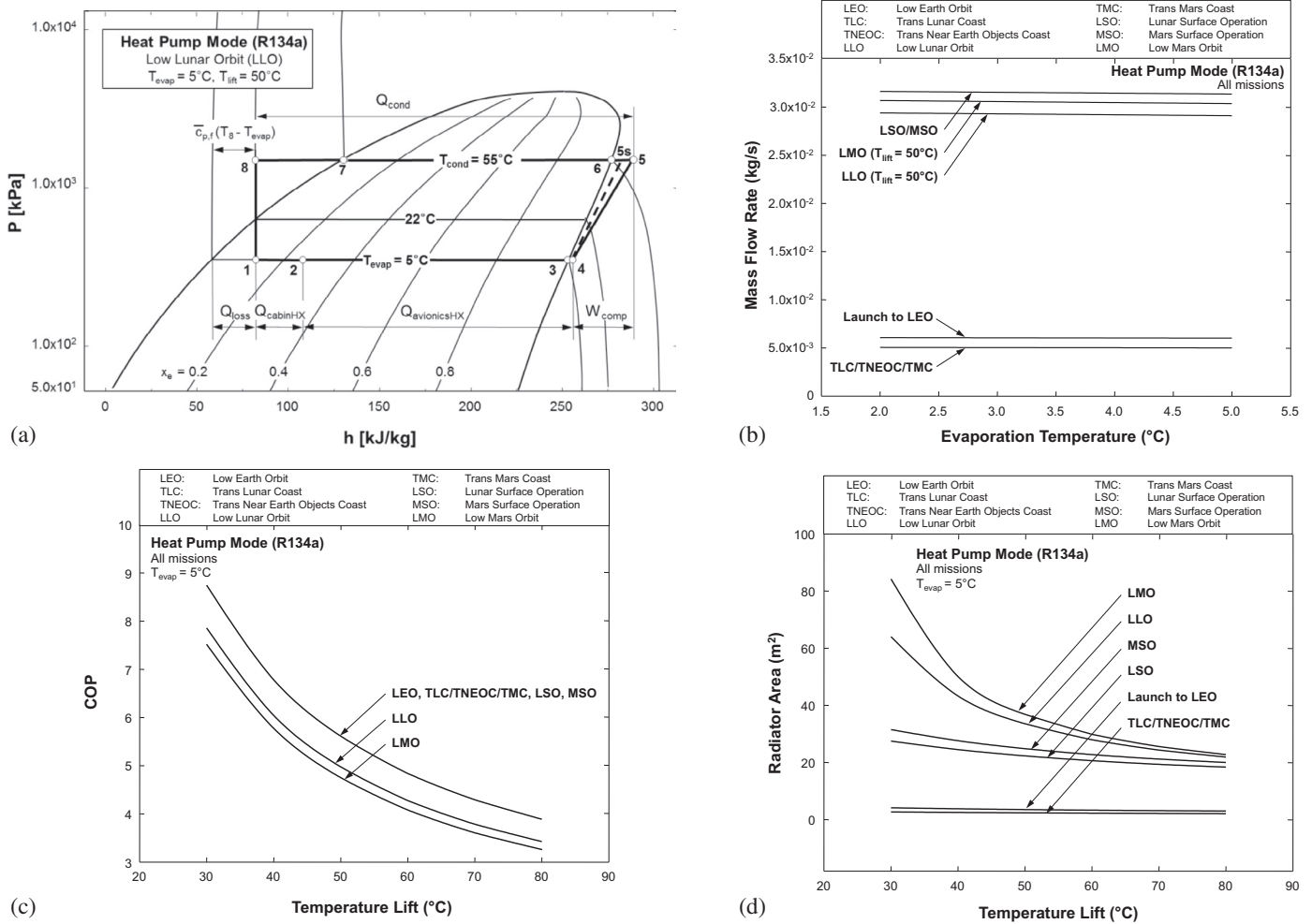
Fig. 12. Thermodynamic results for basic heat pump mode using R134a: (a) *P-h* diagram for LLO. (b) Variation of mass flow rate with evaporation temperature for all mission stages. (c) Variation of COP with lift temperature for all mission stages. (d) Variation of radiator area with lift temperature for all mission stages.

As discussed earlier, the mass flow rate for the two-phase mode is much smaller than for the single-phase mode because of the reliance on latent heat rather than sensible heat. However, two-phase flow is associated with higher pressure drop than single-phase flow for the same mass flow rate. This increase, which increases pump work, is caused by increases in the frictional and accelerational pressure gradients throughout the TCS. In addition, as discussed earlier, the two-phase mode requires a larger radiator area.

5.3. Thermodynamic analysis for heat pump mode using R134a

Discussed here are two types of heat pump cycles using R134a as working fluid, a basic heat pump cycle and a cycle that is augmented with a LLSL-HX. For the basic cycle, the maximum temperature lift is limited by the condenser's saturation temperature, which should be lower than the fluid's critical temperature. With a critical temperature for R134a of 100.9 °C (corresponding to 40.6 bar), a maximum temperature lift of 80 °C in the analysis below ensures a discharge temperature of 98.47 °C, which is below the thermal decomposition temperature of 250 °C. Increasing the lift temperature increases compressor work, decreases COP, and decreases radiator area. As a trade-off, an intermediate temperature lift of 50 °C is used to illustrate a basic heat pump cycle's normal operation.

A *P-h* diagram for the basic heat pump cycle is shown in Fig. 12(a) for Low Lunar Orbit (LLO) with evaporator temperature and temperature lift of 5 and 50 °C, respectively, and a corresponding condenser temperature of 55 °C. Table 6 provides values for key cycle parameters along with the thermodynamics relations used for analysis of the basic heat pump cycle for LLO. Heat transfer to the fluid in the cabin heat exchanger at $Q_{cabinHX} = 0.75$ kW increases enthalpy from state 1 to state 2 as shown in Fig. 12(a). Additional heat transfer in the avionics heat exchanger at $Q_{avionicsHX} = 4.25$ kW increases enthalpy from 2 to 3. This is followed by 1 °C superheating between 3 and 4, compression from 4 to 5, condensation from 5 to 8, and throttling from 8 to 1. State 5s is the isentropic discharge state. In the condenser, the fluid rejects the heat to the environment by radiation, and is converted from saturated vapor at 6 ($x_e = 1$) to saturated liquid at 7 ($x_e = 0$), and the liquid is then subcooled between 7 and 8.

The condenser's outlet temperature, T_8, is limited by the heat sink temperature and minimum condenser pinch temperature. With a heat sink temperature of 17 °C and minimum pinch temperature of 5 °C, the minimum condenser outlet temperature for LLO is 22 °C. This determines state 8 and therefore the maximum amount of subcooling in the condenser. Because isothermal lines to the left of the saturated liquid line are nearly vertical, the 'loss of subcooling' resulting from the 22 °C limit can be approximated by [39]

Table 6
Fluid states indicated in *P-h* and *T-s* diagrams for basic heat pump mode and heat pump with LLSL-HX mode using R134a.

Evaporation temperature: $T_{evap} = 5$ °C
Superheat at evaporator exit: $T_{super} = 1$ °C
Lift temperature: $T_{lift} = 50$ °C
Sink temperature (LLO): $T_{sink} = 17$ °C
Minimum condenser outlet temperature (LLO): $T_{cond,out} = 22$ °C
Cabin cooling load (LLO): $Q_{cabinHX} = 0.75$ kW
Avionics cold plates' cooling load (LLO): $Q_{avionicsHX} = 4.25$ kW
Coefficient of performance: $COP = (Q_{cabinHX} + Q_{avionicsHX})/(W_{comp,isentropic}/\eta_{comp})$
Evaporation pressure: $P_{evap} = P_{sat}(T_{evap})$
Condensation pressure: $P_{cond} = P_{sat}(T_{cond}) = P_{sat}(T_{evap} + T_{lift})$

A. Compressor
  Inlet temperature: $T_4 = T_{evap} + T_{super}$
  Inlet pressure: $P_4 = P_{evap}$
  Inlet enthalpy: $h_4 = h(T_4, P_4)$
  Inlet entropy: $s_4 = s(T_4, P_4)$
  Discharge pressure: $P_5 = P_{cond}$
  Isentropic discharge entropy: $s_{5s} = s_4$
  Isentropic discharge enthalpy: $h_{5s} = h(P_5, s_{5s})$
  Real discharge enthalpy: $h_5 = h_4 + (h_{5s} - h_4)/\eta_{comp}$
  Compressor efficiency: $\eta_{comp} = 0.85$
  Discharge temperature: $T_5 = T(P_5, h_5)$
  Real discharge entropy: $s_5 = s(P_5, h_5)$
  Compressor work: $W_{comp} = \dot{m}(h_5 - h_4)$

B. Condenser
  Outlet temperature: $T_8 = T_{sink} + \Delta T_{cond,pinch}$
  Outlet pressure: $P_8 = P_{cond}$
  Outlet enthalpy: $h_8 = h(T_8, P_8)$
  Outlet entropy: $s_8 = s(T_8, P_8)$

C. Throttling valve
  Isenthalpic expansion through valve: $h_1 = h_8$

D. Evaporator
  Cabin HX inlet temperature: $T_1 = T_{evap}$
  Cabin HX inlet pressure: $P_1 = P_{evap}$
  Cabin HX inlet enthalpy: $h_1 = h_8$
  Cabin HX inlet entropy: $s_1 = s(P_1, h_1)$
  Cabin heat exchanger heat load: $Q_{cabinHX} = \dot{m}(h_2 - h_1)$
  Avionics heat exchanger heat load: $Q_{avionicsHX} = \dot{m}(h_4 - h_2)$

E. Saturation states
  Vapor saturation point in avionics cold plates: $T_3 = T(P_{evap}, x_e = 1)$
  Vapor saturation point in condenser: $T_6 = T(P_{cond}, x_e = 1)$
  Liquid saturation point in condenser: $T_7 = T(P_{cond}, x_e = 0)$

F. Heat pump with LLSL-H/X
  Maximum regenerative enthalpy exchange:
    $\Delta h_{reg,max} = \min\{h_g - h(T_4, P_8), h(T_8, P_4) - h_4\}$
  Actual regenerative enthalpy exchange: $\Delta h_{reg} = \varepsilon_{reg} \Delta h_{reg,max}$
  Effectiveness of regenerator: $\varepsilon_{reg} = 0.90$
  Compressor inlet enthalpy: $h_4 = h_4 + \Delta h_{reg}$
  Condenser outlet enthalpy: $h_8 = h_8 - \Delta h_{reg}$

$$Q_{loss} = \dot{m}_{hp} \bar{c}_{p,f}(T_8 - T_{evap}) \tag{16}$$

Maximizing the condenser's subcooling is recommended to reduce this loss in cooling capacity.

Figure 12(b) shows that the mass flow rate for R134a for the heat pump mode decreases slightly with increasing evaporation temperature. LSO/MSO requires the highest mass flow rate because heat load is highest for these mission stages. Also, despite having to tackle equal heat loads, LMO requires a slightly higher flow rate than LLO because of the higher heat sink temperature for the former.

Figure 12(c) shows heat pump COP for R134a decreases with increasing temperature lift because of increasing compressor work. Here, COP is defined as

$$COP = \frac{Q_{cabinHX} + Q_{avionicsHX}}{W_{comp}} = \frac{h_4 - h_1}{h_5 - h_4} \tag{17}$$

In Eq. (17), increasing the temperature lift increases the compressor's discharge enthalpy, h_5, therefore increasing compressor work, $h_5 - h_4$, which decreases COP.

Figure 12(d) shows the radiator area for R134a decreases with increasing lift temperature and therefore increasing condenser temperature. Notice that LMO and LLO require large radiator areas because of their high heat loads and high sink temperatures.

5.4. Thermodynamic analysis of heat pump with liquid-line to suction-line heat exchanger (LLSL-HX) mode using R134a

Using a counterflow heat exchanger to transfer heat from hot liquid at the condenser outlet to cold vapor at the evaporator outlet has been commonly used to enhance heat pump cooling capacity [25,39,40]. The LLSL-HX increases both the superheat at the compressor inlet and subcooling at the condenser outlet, the latter also decreases the enthalpy of fluid entering the evaporator. Figure 13(a) shows a *P-h* diagram for a heat pump with LLSL-HX mode using R134a for Low Mars Orbit (LMO). Shown in this figure are two additional steps of regenerative heat exchange, 4 to 4′ at the compressor inlet and 8 to 8′ at the condenser outlet, compared to a basic heat pump.

Figure 13(b) shows a *T-s* diagram for a heat pump with LLSL-HX mode using R134a for LMO. Table 6 provides values for key cycle parameters along with the thermodynamics relations used for analysis of the heat pump with LLSL-HX mode. The enthalpy of cold vapor, h_4, is higher than the enthalpy of hot liquid, h_8, so it is assumed that the heat exchange occurs at the same pressure (P_4 or P_8) but different temperatures. With the LLSL-HX, the condenser outlet temperature can decrease below the temperature limit of 27 °C for LMO, which enhances cooling capacity. The amounts of superheat at the compressor inlet and subcooling at the condenser outlet depend on the regeneration effectiveness of the LLSL-HX; an effectiveness value of 0.90 is used in the present analysis [25]. Figure 13(c) shows the mass flow rate of R134a decreases by virtue of the enhanced cooling capacity provided by the LLSL-HX.

Figure 14(a) shows the variation of COP with temperature lift for a basic heat pump mode and heat pump with LLSL-HX mode for LLO and LMO using R134a. Notice how the LLSL-HX decreases COP because the compressor work increases more than the saving in mass flow rate.

Overall, the influence of the LLSL-HX on COP is governed by three parameters, regeneration effectiveness, subcooling at the condenser outlet, and superheating at the compressor inlet. Figure 14(b) shows the influence of subcooling at the condenser outlet on the difference in coefficient of performance, COP′ – COP, between the heat pump with LLSL-HX mode and basic heat pump mode for LLO, while fixing evaporation temperature, compressor efficiency and regeneration effectiveness at 5 °C, 0.85 and 0.9, respectively. Subcooling is measured in Fig. 13(a) and (b) from point 7, where the condensing two-phase mixture is converted completely to liquid, and the subcooling is limited by the condenser's saturation temperature and condenser bottom temperature limit. For LMO, a temperature lift of 50 °C results in a condensation temperature of 55 °C, and, with the lower limit of 27 °C imposed by the 22 °C heat sink temperature, the maximum subcooling is 28 °C. For LLO, with a lower limit of 22 °C imposed by the 17 °C heat sink temperature, the maximum subcooling is 33 °C. Figure 14(b) shows that the LLSL-HX becomes less effective with increasing subcooling and, for a 50 °C lift, the LLSL-HX is beneficial for subcoolings below 25 °C. The effectiveness of the LLSL-HX also increases with increasing temperature lift. Figure 14(c) shows cooling performance is enhanced with increasing effectiveness. Figure 14(d) compares radiator area for the heat pump with LLSL-HX mode with that for the basic heat pump. The LLSL-HX is shown decreasing radiator area slightly by virtue of higher compressor discharge temperature.

Thermodynamic evaluation of the performance of LLSL-HX was conducted by Domanski et al. [39] to assess the influence of dif-
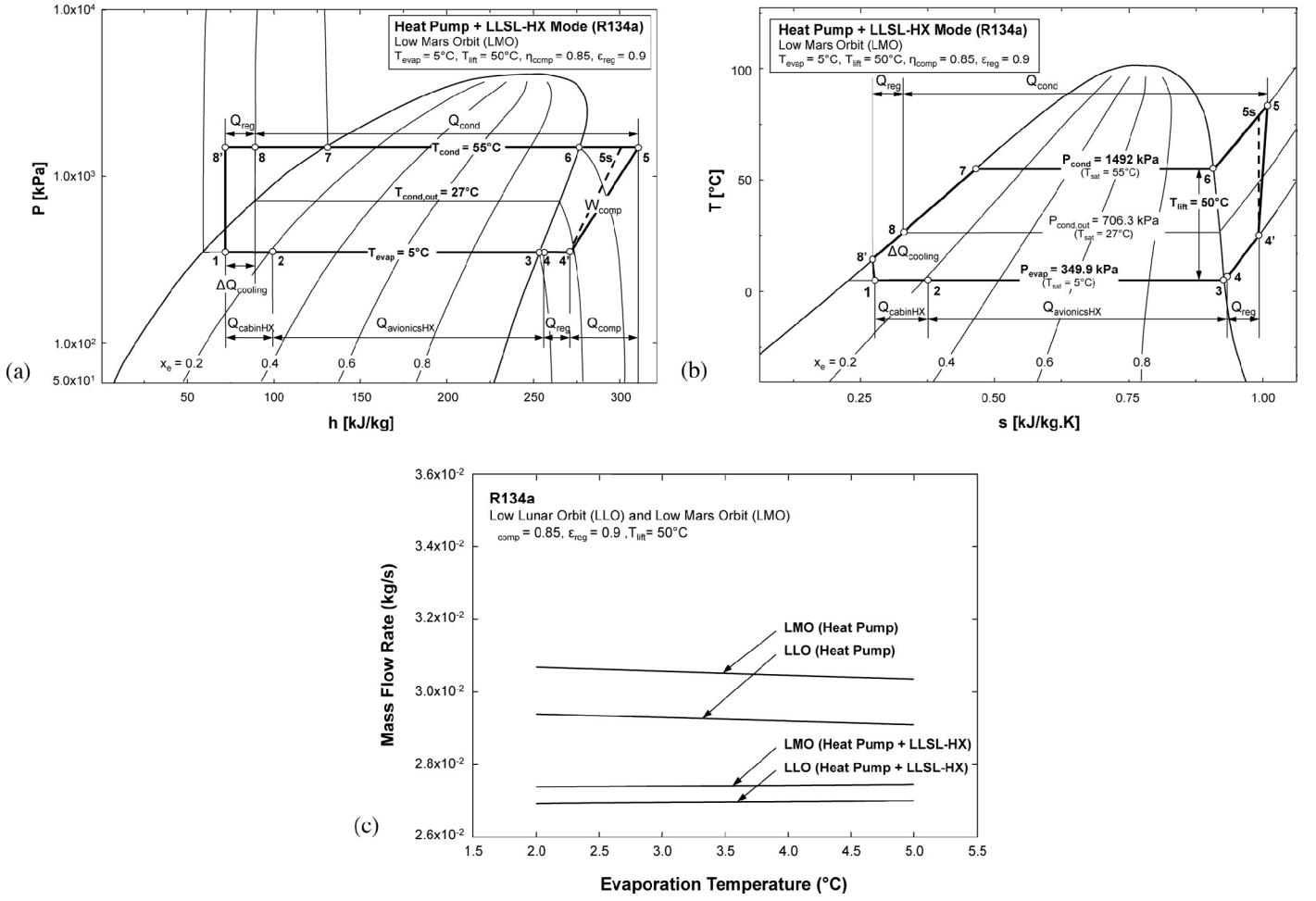
Fig. 13. Thermodynamic results for heat pump with LLSL-HX mode using R134a: (a) *P-h* diagram for LMO and (b) *T-s* diagram for LMO. (c) Variations of mass flow rate for LMO and LLO for basic heat pump mode and heat pump with LLSL-HX mode.

ferent operating variables. The following are key relations used in their assessment.

$$COP = \frac{Q_{cabinHX} + Q_{avionicsHX}}{W_{comp}} \tag{18}$$

and

$$COP' = \frac{(Q_{cabinHX} + Q_{avionicsHX}) + \Delta Q_{cooling}}{W_{comp} + \Delta W_{comp}}$$

$$= \left[\frac{1 + \left\{ \frac{\Delta Q_{cooling}}{Q_{cabinHX} + Q_{avionicsHX}} \right\}}{\left\{ 1 + \frac{\Delta W_{comp}}{W_{comp}} \right\}} \right] COP \tag{19}$$

Applying a Taylor series expansion to the denominator and neglecting higher order terms,

$$COP' \cong \left[1 + \left\{ \frac{\Delta Q_{cooling}}{Q_{cabinHX} + Q_{avionicsHX}} \right\} - \left\{ \frac{\Delta W_{comp}}{W_{comp}} \right\} \right] COP \tag{20}$$

Equation (20) indicates $COP' > COP$ when the cooling enhancement ratio exceeds the ratio of added compressor work.

The regeneration efficiency is expressed as [39,40]

$$\varepsilon_{reg} = \frac{\bar{c}_{p,g}(T_{4'} - T_4)}{Min\{\bar{c}_{p,g}, \bar{c}_{p,f}\}(T_8 - T_4)} = \frac{T_{4'} - T_4}{T_8 - T_4} \tag{21}$$

because $\bar{c}_{p,g} < \bar{c}_{p,f}$, where

$$T_4 = T_{evap} + \Delta T_{super} \tag{22}$$

The cooling capacity can be expressed as $Q_{cooling} = \dot{m}_{hp}\{h_{fg}(T_{evap}) + \Delta h_{super}\} - Q_{loss}$, where Q_{loss} is given by Eq. (16). Therefore

$$\begin{aligned} Q_{cooling} &= \dot{m}_{hp}\{h_{fg}(T_{evap}) + \Delta h_{super}\} - \dot{m}_{hp}\bar{c}_{p,f}(T_8 - T_{evap}) \\ &= \dot{m}_{hp}\{h_{fg}(T_{evap}) + \Delta h_{super}\} - \dot{m}_{hp}\bar{c}_{p,f}(T_8 - T_4 + \Delta T_{super}) \\ &= \dot{m}_{hp}\{h_{fg}(T_{evap}) - \bar{c}_{p,f}(T_8 - T_4)\}, \end{aligned} \tag{23}$$

where $\Delta h_{super} = \bar{c}_{p,g}\Delta T_{super}$ and $h_{fg}(T_{evap}) - \bar{c}_{p,f}(T_8 - T_4) \gg (\bar{c}_{p,f} - \bar{c}_{p,g})\Delta T_{super}$.

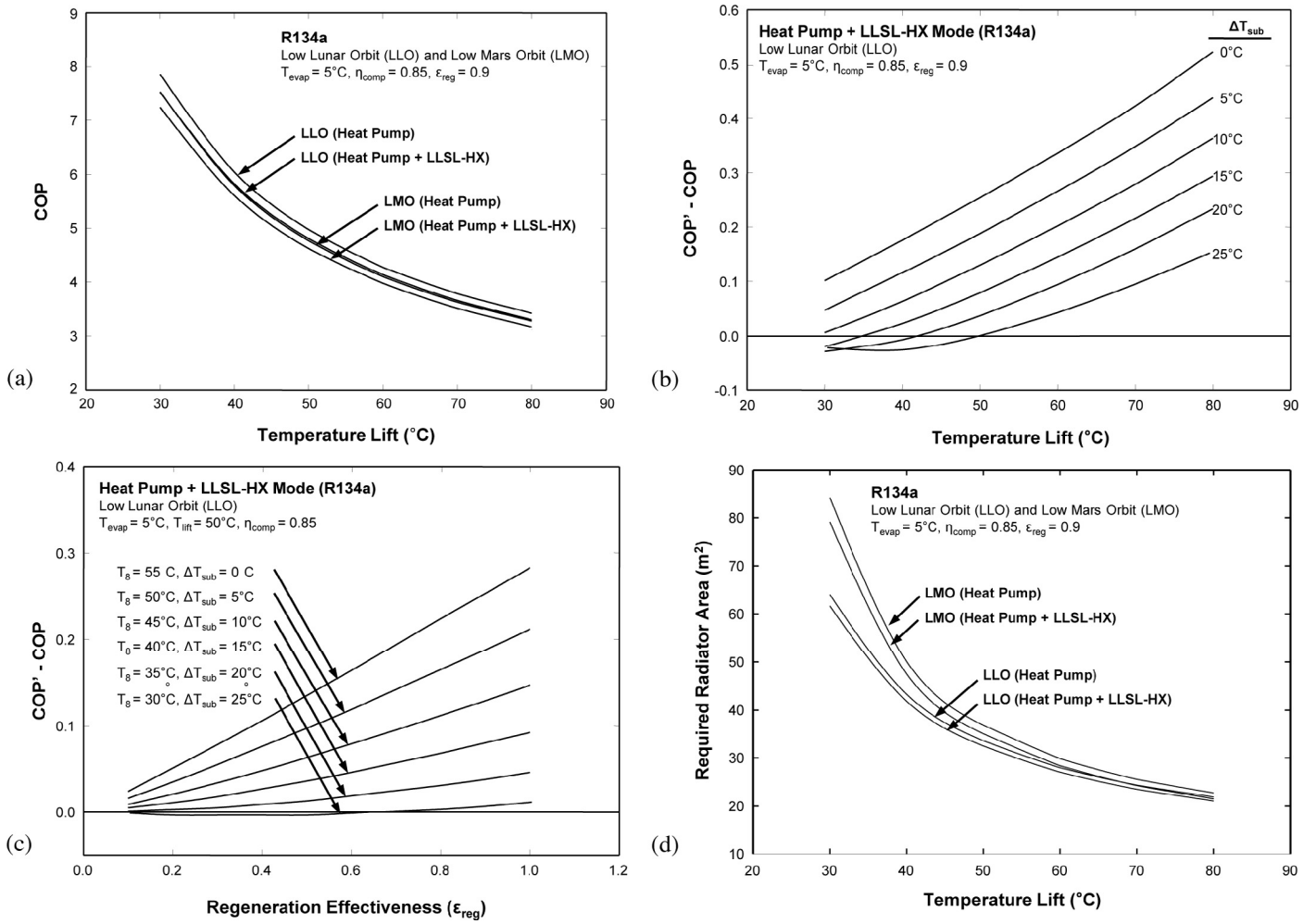In Eq. (23),

$$\bar{c}_{p,f} = \frac{1}{T_8 - T_{evap}} \int_{T_{evap}}^{T_8} c_{p,f} dT \tag{24}$$

and the enhancement in cooling rate is given by

$$\Delta Q_{cooling} = \bar{c}_{p,g}(T_{4'} - T_4) = \varepsilon_{reg}\bar{c}_{p,g}(T_8 - T_4) \tag{25}$$

where

$$\bar{c}_{p,g} = \frac{1}{T_{4'} - T_4} \int_{T_4}^{T_{4'}} c_{p,g} dT \tag{26}$$

Fig. 14. (a) COP for basic heat pump mode and heat pump with LLSL–HX mode for LLO and LMO using R134a. (b) Variation of COP enhancement due to LLSL–HX with temperature lift for LLO using R134a. (c) Variation of COP enhancement due to LLSL–HX with regenerative effectiveness for LLO using R134a. (d) Variation of radiator area with temperature lift for basic heat pump mode and heat pump with LLSL–HX mode for LLO and LMO using R134a.

Therefore, the cooling enhancement is a function of ε_{reg}, T_8 and T_4.

The compressor work can be determined by multiplying isentropic compression, where the vapor is assumed an ideal gas with constant heat capacity ratio, by compression efficiency.

$$W_{comp} = \eta_{comp} \left(\frac{k}{k-1}\right)\left[\left(\frac{P_5}{P_4}\right)^{(k-1)/k} - 1\right]\dot{m}_{hp}P_4 v_4 \tag{27}$$

and $$W'_{comp} = \eta_{comp} \left(\frac{k}{k-1}\right)\left[\left(\frac{P_{5'}}{P_{4'}}\right)^{(k-1)/k} - 1\right]\dot{m}_{hp}P_4 v_{4'} \tag{28}$$

where $k = c_{p,g}/c_{v,g}$, $P_{5'} = P_5$ and $P_{4'} = P_4$. Therefore

$$\Delta W_{comp} = W'_{comp} - W_{comp}$$

$$= \eta_{comp} \left(\frac{k}{k-1}\right)\left[\left(\frac{P_5}{P_4}\right)^{(k-1)/k} - 1\right]\dot{m}_{hp}P_4 (v_{4'} - v_4) \tag{29}$$

Combining Eqs. (23), (25), (27) and (29) into Eq. (20) yields

$$\frac{COP'}{COP} \cong \frac{\left[1 + \left\{\frac{\varepsilon_{reg}\bar{c}_{p,g}(T_8 - T_4)}{\{h_{fg}(T_{evap}) - \bar{c}_{p,f}(T_8 - T_4)\}}\right\}\right]}{1 + \frac{v_{4'} - v_4}{v_4}} \tag{30}$$

Introducing the coefficient of thermal expansion, which is defined as

$$\beta_v = \frac{1}{v}\left(\frac{\partial v}{\partial T}\right)_P \cong \frac{v_{4'} - v_4}{v_4(T_{4'} - T_4)} \tag{31}$$

in Eq. (30), and applying Eq. (21) yields

$$\frac{COP'}{COP} \cong \frac{\left[1 + \varepsilon_{reg}(T_8 - T_4)\left\{\frac{\bar{c}_{p,g}}{h_{fg}(T_{evap}) - \bar{c}_{p,f}(T_8 - T_4)}\right\}\right]}{1 + (T_8 - T_4)\beta_v} \tag{32}$$

For R134a and LMO mission, $\bar{c}_{p,g} = 0.9125\,\text{kJ/kg·K}$, $h_{fg}(T_{sat}) = 194.8\,\text{kJ/K}$, and $\beta_v = 4.615 \times 10^{-3}\,\text{K}^{-1}$. Figure 14(c) shows, for LLO, COP′ – COP versus ε_{reg} for different subcoolings. It shows the enhancement due to the LLSL–HX increases with increasing ε_{reg} and decreasing subcooling brought about by increasing T_8.

5.5. Comparison of different modes

The mass flow rate comparison among the different operation modes of H-TCS for different heat loads and heat sink temperatures is not sufficient to pinpoint the optimal mode. Additional information is required about pump and/or compressor work to determine the mode corresponding to minimum work input. The
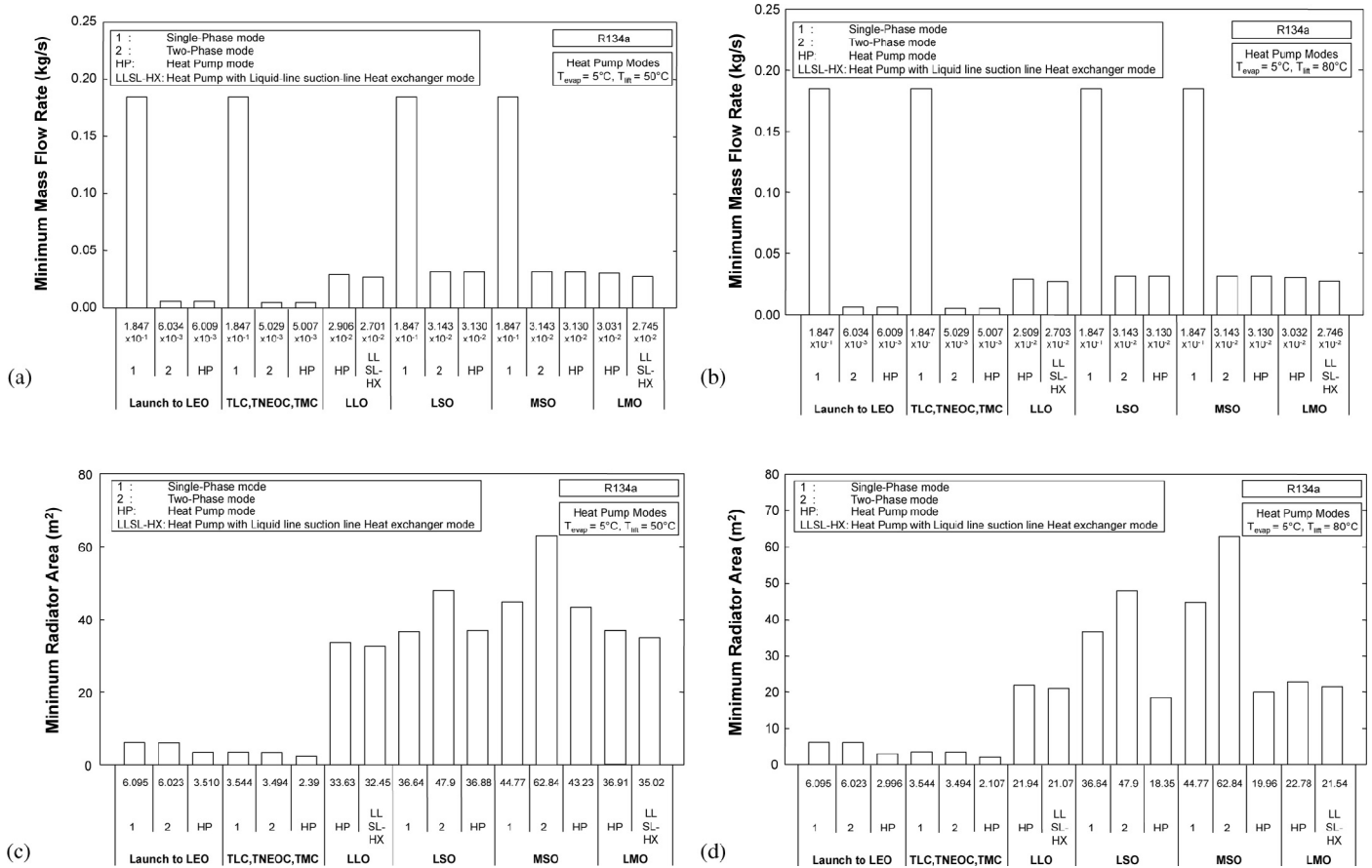
Fig. 15. Comparison of minimum mass flow rate for temperature lifts of (a) 50 °C and (b) 80 °C, and minimum radiator area for temperature lifts of (c) 50 °C and (d) 80 °C for different mission stages using R134a as working fluid.

thermodynamic analysis presented in this study does not account for pressure drop. A complete assessment of system performance must account for pressure drop in the evaporator and condenser and in the adiabatic tubing to determine pump work and total work input. However, such assessment will require detailed information on tubing diameter and length for the entire loop.

Figure 15(a) and (b) compares the minimum mass flow rate for the four modes and different mission stages using R134a as working fluid with temperature lifts of 50 and 80 °C. Notice that the mass flow rate for the heat pump mode is slightly smaller than for the two-phase mode because of the evaporator superheat of 1 °C for the former. But the flow rate for the single-phase mode is significantly greater because of its reliance on sensible heat alone. The mass flow rate for the basic heat pump mode and heat pump with LLSL-HX mode with an 80 °C temperature lift is slightly higher than with a 50 °C lift in LMO/LLO because of higher condenser outlet enthalpy for the 80 °C lift. The cooling capacity, which is determined by the difference between inlet and outlet enthalpy, is reduced by the higher condenser outlet enthalpy from the higher pressure for 80 °C lift, and the throttling maintains the enthalpy up to the evaporator inlet. Reduced cooling capacity leads to a higher mass flow requirement.

Radiator area has a very strong bearing on spacecraft weight and must therefore be as small as possible. Figure 15(c) and (d) compares the radiator area for the different modes and different mission stages using R134a with temperature lifts of 50 and 80 °C. Because the single-phase and two-phase modes cannot be used with high sink temperature missions (LLO and LMO), these missions are tackled

only by the heat pump modes. The radiator area is dictated by a combination of highest thermal load and highest sink temperature, which correspond to LMO. Notice in Fig. 15(c) and (d) that, for all missions, this area is larger for the heat pump mode than for the single-phase and two-phase modes, but slightly smaller when employing the LLSL-HX. Therefore, the radiator area of 35.02 m² for $T_{lift} = 50$ °C and 21.54 m² for $T_{lift} = 80$ °C for LMO using the heat pump with LLSL-HX mode dictate radiator area for all modes and mission stages. Overall, the radiator area should be based on the heat pump mode with LLSL-HX and LMO with a temperature lift of 80 °C, which is 21.54 m². For missions where radiator area associated with the single-phase or two-phase modes exceeds 21.54 m² (LSO and MSO), the H-TCS would switch from these modes to the heat pump with LLSL-HX mode to take advantage of the smaller radiator area.

Figure 16(a) and (b) shows, for R134a, the variation of maximum sink temperature that the single-phase and two-phase modes can tackle with total heat load, with the radiator area based on heat pump mode and LMO in Fig. 16(a) and heat pump with LLSL-HX mode and LMO in Fig. 16(b) for different lift temperatures. Note that the operation mode must be switched into one of the two heat pump modes when the radiator size is insufficient for the single or two-phase modes. Because of its lower temperatures, the two-phase mode requires lower sink temperatures than the single-phase mode, and the heat sink temperature difference between the two modes increases with increasing heat load. The rate of required sink temperature decrease for the single-phase mode is alleviated with increased surface temperature as the heat load increases, while the surface temperature for the two-phase mode is limited by the evap-
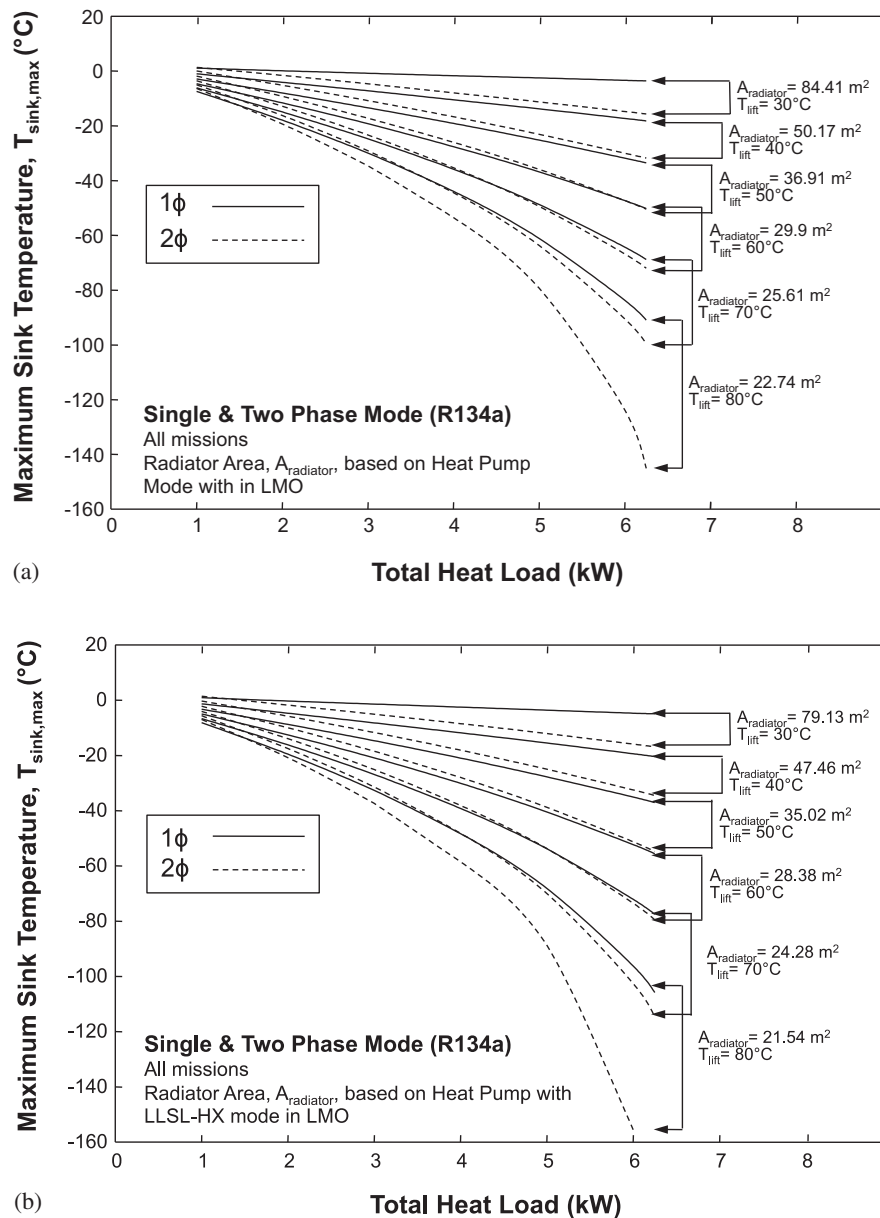
Fig. 16. Variation of maximum heat sink temperature with avionics heat load for single-phase and two-phase modes and all mission stages for different combinations of radiator area and temperature lift, with radiator area based on (a) basic heat pump mode and LMO, and (b) heat pump with LLSL-HX mode and LMO, using R134a as working fluid.

orator saturation temperature, $T_{evap} = 5$ °C. Figure 16(a) and (b) shows that the single-phase and two-phase modes can be used when the avionics heat load is low or heat sink temperature is low.

6. Conclusions

This paper examined the development of a single-loop, hybrid thermal control system (H-TCS) for the Multi-Purpose Crew Vehicle (MPCV) for different future space missions and mission stages. A detailed thermodynamic methodology is used to assess the suitability of four possible modes of operation (single-phase, two-phase, basic heat pump and heat pump with LLSL-HX) and six working fluids at meeting the thermal requirements and enduring the operating environments of the different missions. Key findings from the study are as follows:

1. Among the six working fluids that were evaluated relative to different performance parameters, R134a is deemed most suitable based on its ability to provide a balanced compromise between reducing flow rate and maintaining low pressure. R134a also offers moderate coefficient of performance (COP) and low accelerational pressure drop, is both nontoxic and nonflammable, and features zero ozone depletion potential (ODP) and low global warming potential (GWP).

2. The single-phase mode requires the highest coolant mass flow rate because of its reliance on sensible heat alone. The two-phase and heat pump modes greatly reduce mass flow rate compared to the single-phase mode because of their reliance on both sensible and latent heat. Among the different mission stages, Lunar Surface Operation (LSO) and Mars Surface Operation (MSO) account for the highest heat load of 6.25 kW and therefore require the highest R134a mass flow rates: 1.85×10^{-1} kg/s

for single-phase mode, 3.14×10^{-2} kg/s for two-phase mode, and 3.13×10^{-2} kg/s for basic heat pump mode.

3. Operating pressure has a strong bearing on TCS weight via hardware mass and piping thickness, and R134a shows moderate pressure ratings compared to other fluids. The highest system pressure is determined by LSO/MSO for single-phase/two-phase modes, and by Low Lunar Orbit/Low Mars Orbit (LLO/LMO) for both heat pump modes. For R134a, H-TCS requires different pressure ratings for the different operation modes: 6.936 bar for single-phase, 3.497 bar for two-phase, and 26.332 bar for basic and LLSL-HX heat pump modes.

4. The orbital missions LLO and LMO are associated with the highest heat sink temperatures, which exceed the heat acquisition temperature in H-TCS. Therefore, only the basic heat pump mode and heat pump with LLSL-HX mode are capable of tackling these two mission stages. The heat pump with LLSL-HX mode requires the smallest radiator area of 21.54 m^2 for R134a and a temperature lift of 80 °C, while the basic heat pump mode requires a radiator area of 22.78 m^2 for R134a and a temperature lift of 80 °C.

5. For the basic heat pump mode and heat pump with LLSL-HX mode, there is a trade-off in selecting temperature lift. Increasing the temperature lift increases compressor work while reducing radiator surface area because of higher radiator temperature. For the heat pump with LLSL-HX, increasing the temperature lift for LMO from 30 to 80 °C decreases COP from 7.2 to 3.2 while decreasing the radiator area from 79.13 to 21.54 m^2.

Acknowledgement

Nomenclature

A	area
A_{liquid}	condensing radiator area occupied by liquid
$A_{radiator}$	radiator area
A_{sat}	condensing radiator area occupied by two-phase mixture
A_{vapor}	condensing radiator area occupied by vapor
c_p	specific heat at constant pressure
c_v	specific heat at constant volume
COP	coefficient of performance of basic heat pump
COP'	coefficient of performance of heat pump with LLSL-HX
D	tube diameter
h	enthalpy
h_{fg}	latent heat of vaporization
k	specific heat ratio; thermal conductivity
$\dot{m}$	mass flow rate
P	pressure
P_r	reduced pressure
Pr	Prandtl number
Q	heat transfer rate (heat load)
$Q_{cooling}$	cooling capacity
Q_{loss}	loss of cooling capacity
q'	heat transfer rate per unit tube length
q_v	volumetric capacity
s	entropy
T	temperature
T_{lift}	temperature lift from evaporator to condenser
T_{sink}	heat sink temperature
V	volume
v	specific volume
v_{fg}	specific volume difference between vapor and liquid
W_{comp}	compressor work input
x_e	thermodynamic equilibrium quality
z	coordinate along flow direction

Greek symbols

α	absorptivity
β_v	coefficient of thermal expansion
ε	emissivity
ε_{reg}	regeneration effectiveness
η_{comp}	compressor efficiency
μ	viscosity
ρ	density
σ	Stephan–Boltzmann constant; surface tension

Subscripts

A	accelerational
$avionicsHX$	avionics heat exchanger
$cabin$	cabin
$cabinHX$	cabin heat exchanger
$comp$	compressor
$cond$	condenser
$crit$	critical
$evap$	evaporator (cabin HX plus avionics HX)
f	liquid
g	vapor
hp	heat pump
in	inlet
$lift$	lift
max	maximum
min	minimum
out	outlet
$pinch$	pinch temperature difference
$radiator$	condensing radiator
reg	regenerator (LLSL-HX)
s	surface
sat	saturation
$super$	superheating
1ϕ	single-phase
2ϕ	two-phase

Acronyms

CEV	Crew Exploration Vehicle
EDS	Earth Departure Stage
GWP	Global Warming Potential
H-TCS	Hybrid Thermal Control System
ISS	International Space Station
LEO	Low Earth Orbit
LLO	Low Lunar Orbit
LLSL-HX	Liquid-Line Suction-Line Heat Exchanger
LMO	Low Mars Orbit
LSAM	Lunar Surface Access Module
LSO	Lunar Surface Operation
MPCV	Multi-Purpose Crew Vehicle
MSO	Mars Surface Operation
NEO	Near Earth Object
ODP	Ozone Depletion Potential
SLR	Space Launch System
TCS	Thermal Control System
TLC	Trans Lunar Coast
TMC	Trans Mars Coast
TNEOC	Trans Near Earth Objects Coast

References

[1] J.F. Connolly, Constellation Program Overview, NASA Report/Presentation NASA Johnson Space Center, Houston, TX, 2006.

[2] J.L. Rhatigan, J.M. Hanley, M.S. Geyer, Formulation of NASA's constellation program. NASA Report SP-2007-563, 2007.

[3] P.A. Abell, D.J. Korsmeyer, R.R. Landis, T.D. Jones, D.R. Adamo, D. Morrison, et al., Scientific exploration of near-earth objects via the Orion Crew Exploration Vehicle, Meteor. Planet. Sci. 44 (2009) 1825–1836.

[4] B.G. Drake, Human exploration of Mars design reference architecture 5.0. NASA Report SP-2009-566, 2009.

[5] J.N. Pelton, A new space vision for NASA – and for space entrepreneurs too?, Space Policy 26 (2010) 78–80.

[6] J.A. Singer, Space Launch System (SLS) program overview: advanced development NASA research announcement industry and academia day. NASA Technical Reports Server, 2012.

[7] A.M. Crocker, K.B. Doering, S.A. Cook, F.D. Backhtel, S. St. Germain, M.G. Schaffer, The benefits of advanced booster competition for NASA's space launch system. Proc. 49th AIAA/ASME/SAE/ASEE Joint Propulsion Conf., San Jose, CA, 2013.

[8] M.K. Ewert, P.A. Petete, J. Dzenitis, Active thermal control systems for lunar and Martian exploration. SAE Technical Paper 901243, 1990.

[9] E. Ungar, Single phase vs. two-phase active thermal control systems for space applications – a trade study, AIAA Paper 95-0634. Proc. 33rd Aerospace Science Meeting and Exhibit, Reno, NV, 1995.

[10] G.B. Ganapathi, B. Gani, B. Gajanana, E. Sunada, J. Miller, Two phase vs. single phase thermal loop trades for exploration mission LAT II architecture. SAE Paper 2008-01-1958, 2008.

[11] R.D. Morton, D. Bergeron, K. Hurlbert, M. Ewert, J. Cornwell, Proof of concept high lift heat pump for a lunar base. SAE Paper 981683, 1998.

[12] M.K. Ewert, D.J. Bergeron III, Development of a solar heat pump for space. Proc. ASME 2005 Int. Solar Energy Conf., Orlando, FL, 2005.

[13] F.P. Chiaramonte, J.A. Joshi, Workshop on critical issues in microgravity fluids, transport, and reaction processes in advanced human support technology – final report. NASA Report TM-2004-212940, 2004.

[14] B.S. Singh, M.H. Hasan, Innovative multi-environment, multimode thermal control system. SAE Paper 2007-01-3202, 2007.

[15] S.M. Kim, I. Mudawar, Flow condensation in parallel micro-channels – part 2: heat transfer results and correlation technique, Int. J. Heat Mass Transf. 55 (2012) 984–994.

[16] H. Zhang, I. Mudawar, M.M. Hasan, Flow boiling CHF in microgravity, Int. J. Heat Mass Transf. 48 (2005) 3107–3118.

[17] C. Konishi, I. Mudawar, M.M. Hasan, Investigation of the influence of orientation on critical heat flux for flow boiling with two-phase inlet, Int. J. Heat Mass Transf. 61 (2013) 176–190.

[18] H. Lee, I. Mudawar, M.M. Hasan, Experimental and theoretical investigation of annular flow condensation in microgravity, Int. J. Heat Mass Transf. 61 (2013) 293–309.

[19] J. Lee, I. Mudawar, Two-phase flow in high-heat-flux micro-channel heat sink for refrigeration cooling applications: part I – pressure drop characteristics, Int. J. Heat Mass Transf. 48 (2005) 928–940.

[20] J. Lee, I. Mudawar, Two-phase flow in high-heat-flux micro-channel heat sink for refrigeration cooling applications: part II – heat transfer characteristics, Int. J. Heat Mass Transf. 48 (2005) 941–955.

[21] R.R. Landis, P.A. Abell, D.J. Korsmeyer, D.R. Adamo, E.T. Lu, T.D. Jones, et al., A piloted Orion flight mission to a near-Earth object: a feasibility study. Proc. SpaceOps Conf., Heidelberg, Germany, 2008.

[22] D.O. Stanley, S.A. Cook, J. Connolly, J.M. Hanley, Exploration systems architecture study: overview of architecture and mission operations approach. Proc. SpaceOps Conf., Rome, Italy, 2006.

[23] R.A. Stephan, Overview of the Altair lunar lander thermal control system design and the impacts of global access. Proc. 41st Int. Conf. on Environmental Systems, Portland, OR, 2011.

[24] R.A. Stephan, Private communication, game changing development program. NASA Headquarters, Washington, DC, 2015.

[25] I.H. Bell, E.A. Groll, J.E. Braun, Performance of vapor compression systems with compressor oil flooding and regeneration, Int. J. Refrigeration 34 (2011) 225–233.

[26] G.S. Cole, R.P. Scaringe, L.R. Grzyll, M.K. Ewert, Development of a gravity-insensitive heat pump for Lunar applications. Proc. Space Tech. and Applications Int. Forum (STAIF), Albuquerque, NM, 2007.

[27] I.H. Bell, E.A. Groll, J.E. Braun, W.T. Horton, Impact of oil solubility and refrigerant flashing on the performance of transcritical CO2 vapor compression systems with oil flooding and regeneration. Proc. Int. Refrigeration Air Conditioning Conf., West Lafayette, IN, 2010.

[28] J. Hugenroth, J. Braun, E. Groll, G. King, Liquid-flooded Ericsson cycle cooler: part 1 – thermodynamic analysis. Proc. Int. Refrigeration Air Conditioning Conf., West Lafayette, IN, 2006.

[29] Y.M. Kim, D.K.K. Shin, J.H.H. Lee, A new Ericsson cycle comprising a scroll expander and a scroll compressor for power and refrigeration applications. Proc. Int. Refrigeration Air Conditioning Conf., West Lafayette, IN, 2004.

[30] A. Hiwata, N. Lida, Y. Futagami, K. Sawai, N. Ishii, Performance investigation with oil-injection to compression chambers on CO2-scroll compressor. Proc. Int. Compressor Engineering Conf., West Lafayette, IN, 2002.

[31] E.W. Lemmon, M.L. Huber, M.O. McLinden, NIST Standard Reference Database 23: NIST Reference Fluid Thermodynamic and Transport Properties – REFPROP, Version 8.0, National Institute of Standards and Technology, Gaithersburg, MD, 2010.

[32] S.A. Klein, Engineering equation solver (EES). F-chart software, Madison, WI, 2010.

[33] M.B. Bowers, I. Mudawar, High flux boiling in low flow rate, low pressure drop mini-channel and micro-channel heat sinks, Int. J. Heat Mass Transf. 37 (1994) 321–332.

[34] M.B. Bowers, I. Mudawar, Two-phase electronic cooling using mini-channel and micro-channel heat sinks: part 2 – flow rate and pressure drop constraints, J. Electr. Packag. – Trans. ASME 116 (1994) 298–305.

[35] UN Document, Montreal Protocol on substances that deplete the ozone layer, 1987.

[36] J.R. Sand, S.K. Fischer, Modelled performance of non-chlorinated substitutes for CFC11 and CFC12 in centrifugal chillers, Int. J. Refrigeration 17 (1994) 40–48.

[37] T.J. Wallington, W.F. Schneider, D.R. Worsnop, O.J. Nielsen, J. Sehested, W.J. Debruyn, et al., The environmental impact of CFC replacements HFCs and HCFCs, Environ. Sci. Technol. 28 (1994) 320A–326A.

[38] C. Park, E. Sunada, Vapor compression hybrid two-phase loop technology for lunar surface applications, AIP Confer. Proc. 969 (2008) 37–43.

[39] P.A. Domanski, D.A. Didion, J.P. Doyle, Evaluation of suction-line/liquid-line heat exchange in the refrigeration cycle, Int. J. Refrigeration 17 (1994) 487–493.

[40] S.A. Klein, D.T. Reindl, K. Brownell, Refrigeration system performance using liquid-suction heat exchangers, Int. J. Refrigeration 23 (2000) 588–596.